Hyperthermal reactions of O(p3sP) with hydrogen and methane
by Donna Joan Garton

A dissertation submitted in partial fulfillment of the requirements for the degree of Doctor of Philosophy in Chemistry
Montana State University

Abstract:
Hyperthermal reactions of O(3P) occur at the surfaces and in the exhaust gases of spacecraft that travel through the residual atmosphere of the Earth at high altitudes (200-600 km). These reactions may degrade materials through oxidation and erosion, or they may yield internally excited reaction products which emit radiation and contribute to the "signature" of a rocket plume. Crossed-beams experiments were used to study model reactions of O(3P) with H2, D2, CH4, and CD4 at center-of-mass collision energies in the range 8-75 kcal mol^-1. Interpretation of the experimental results has been strengthened by theoretical calculations carried out by collaborators. A study of the OH scattered flux as a function of collision energy has led to the determination of an experimental excitation function in the threshold region for the O(3P)+H2 → OH+H reaction. The experimental excitation function clearly matched the theoretical prediction, which confirmed that the laser-detonation source produces O(3P) atoms. The excitation function for the O(3P) + H2 reaction and the dynamics of the O(3P) + D2 reaction, observed experimentally for the first time, demonstrate that these reactions proceed mainly on triplet potential energy surfaces, with little or no intersystem crossing. Experiments on the reactions of O(3P) with methane have revealed a previously unobserved reaction pathway, which involves H-atom elimination: O(3P) + CH4 → OCH3 + H. The excitation function for this reaction has been measured, and the reaction barrier has been determined to be □46 kcal mol^-1. In addition, the expected H-atom abstraction reaction, O(3P) + CH4 → CH3 + OH, has been observed, and the dynamics have been investigated. Theoretical calculations identify a triplet-singlet curve crossing below the triplet barrier for the H-atom elimination reaction, but the observed dynamics indicate reaction exclusively on the two lowest-lying triplet surfaces. While it remains to be seen whether intersystem crossing will affect the outcome of other reactions involving hyperthermal atomic oxygen, unknown reactions which have high barriers are likely to be common in extreme environments such as low-Earth orbit, where spacecraft surfaces and exhaust gases suffer high-energy collisions with ambient atomic oxygen.

HYPERTHERMAL REACTIONS OF O(^3P) WITH HYDROGEN AND METHANE

by

Donna Joan Garton

A dissertation submitted in partial fulfillment
of the requirements for the degree

of

Doctor of Philosophy

in

Chemistry

MONTANA STATE UNIVERSITY
Bozeman, Montana

April 2004

APPROVAL

of a dissertation submitted by

Donna Joan Garton

This dissertation has been read by each member of the dissertation committee and has been found to be satisfactory regarding content, English usage, format, citations, bibliographic style, and consistency, and is ready for submission to the College of Graduate Studies.

Lee Spangler _____ 4/16/04
Date

Approved for the Department of Chemistry

Paul A. Grieco _____ 4-16-04
Date

Approved for the College of Graduate Studies

Bruce McLeod _____ 4-19-04
Date

STATEMENT OF PERMISSION TO USE

In presenting this dissertation in partial fulfillment of the requirements for a doctoral degree at Montana State University, I agree that the Library shall make it available to borrowers under rules of the Library. I further agree that copying of this dissertation is allowable only for scholarly purposes, consistent with "fair use" as prescribed in the U.S. Copyright Law. Requests for extensive copying or reproduction of this dissertation should be referred to Bell & Howell Information and Learning, 300 North Zeeb Road, Ann Arbor, Michigan 48106, to whom I have granted "the exclusive right to reproduce and distribute my dissertation in and from microform along with the non-exclusive right to reproduce and distribute my abstract in any format in whole or in part."

Signature 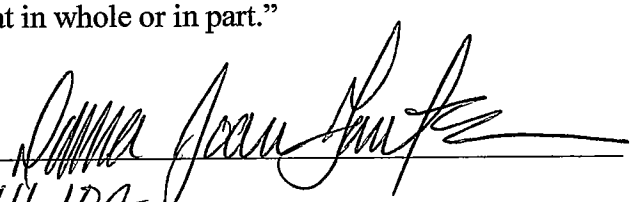

Date 4/16/04

TABLE OF CONTENTS

LIST OF FIGURES vi

ABSTRACT xi

1. INTRODUCTION 1

Spacecraft in the Low-Earth Orbital Environment 1
Polymer Erosion in LEO 2
Chemiluminescence From O-Atom Reactions with Rocket Plumes 3
From LEO to the Laboratory:
Simulating Oxygen Atom Reactions Occurring in LEO 4
Relevant Oxygen Atom Chemistry 5
Oxygen Atom Reactions with Hydrogen 5
Oxygen Atom Reactions with Alkanes 6
Initial Reactions of $O(^3P)$ with a Hydrocarbon Surface 7
Experiment-Theory Coupling 8
References 10

2. METHODS 14

Crossed Molecular Beams Experiments 14
Beam Sources 16
Laser Detonation Source of Hyperthermal Atomic Oxygen 16
Supersonic Beam of Hydrogen and Alkanes 18
Experiment Timing 20
Center-of-Mass to Laboratory Transformation 23
Experimental Resolution 26
References 30

3. EXCITATION FUNCTION FOR THE $O(^3P) + H_2 \rightarrow OH + H$ REACTION: CHARACTERIZATION OF THE OXYGEN ATOM ELECTRONIC STATE IN THE HYPERTHERMAL BEAM 31

Introduction 31
Experimental Details 33
Results and Analysis 35
Discussion 35
Conclusion 40
References 41

TABLE OF CONTENTS - CONTINUED

4. INELASTIC AND REACTIVE SCATTERING DYNAMICS OF $O(^3P) + D_2$ 43

Introduction 43
Experimental Details 47
Results and Analysis 48
Inelastic Scattering 49
Reactive Scattering 52
Discussion 57
Conclusion 63
References 64

5. EXCITATION FUNCTION FOR THE $O(^3P) + CH_4 \rightarrow OCH_3 + H$ REACTION 66

Introduction 66
Experimental Details 68
Results and Analysis 72
Discussion 75
Conclusion 80
References 82

6. INELASTIC AND REACTIVE SCATTERING DYNAMICS OF $O(^3P)$ COLLISIONS WITH CH_4 AND CD_4 84

Introduction 84
Experimental Details 89
Results and Analysis 90
$O(^3P) + CH_4$ 90
$O(^3P) + CD_4$ 94
Relative Yields of Primary Reactive Pathways for $O(^3P) + CH_4$ 107
Reactions Involving Molecular Oxygen 109
Discussion 111
Conclusion 118
References 120

7. CONCLUSION 121

LIST OF FIGURES

Figure Page

2.1. Schematic diagram of the crossed molecular beams apparatus at Montana State University. 15

2.2. Representative oxygen atom beam time-of-flight distributions. The overall beam distribution (dashed line) was narrowed in all of the experiments with the use of a synchronize chopper wheel. 20

2.3. Example timing diagram used in the experiments. 21

3.1. A Newton diagram for the OH + H channel of the $O(^3P) + H_2$ reaction at E_{coll} = 15 kcal mol^{-1}. 32

3.2. Oxygen-atom beam velocity distributions created from chopping the overall beam pulse with a velocity selector wheel rotating at 270 Hz. 34

3.3. Time-of-flight (TOF) distributions of inelastically scattered O (top) and reactively scattered OH (bottom), collected with a detector angle of 5° with respect to the oxygen-atom beam. 36

3.4. Predicted excitation curves (lines) for the $O + H_2$ reaction on singlet and triplet surfaces and experimental data points (circles) for the relative flux of scattered OH product. 37

3.5. Calculated excitation functions from Schatz *et al.* for the $O(^3P) + H_2 \rightarrow$ OH + H reaction. 39

4.1. A Newton diagram showing inelastically scattered O and reactively scattered OD from hyperthermal collisions of $O(^3P)$ with D_2 at E_{coll} = 25 kcal mol^{-1}. 44

4.2. Potential energy curves along the minimum energy path for the triplet reaction with H_2 at slightly bent O-H-H geometries. 46

4.3. Representative time-of-flight distributions of inelastically scattered O following collisions with D_2 at E_{coll} = 25 kcal mol^{-1}. 50

LIST OF FIGURES - CONTINUED

Figure Page

4.4. Laboratory angular distribution of $m/z = 16$ (O^+) inelastically scattered from D_2 with $E_{coll} = 25$ kcal mol^{-1}. 50

4.5. Center-of-mass translational energy distribution for the inelastic scattering of O from D_2 at $E_{coll} = 25$ kcal mol^{-1}, derived from the TOF and laboratory angular distributions for $m/z = 16$ (O^+) through the forward convolution method. 51

4.6. Center-of-mass angular distribution for O atoms that scatter inelastically from D_2 at $E_{coll} = 25$ kcal mol^{-1}, derived from the TOF and laboratory angular distributions for $m/z = 16$ (O^+) through the forward convolution method. 51

4.7. Center-of-mass velocity-flux map superimposed on a Newton diagram for O atoms that scatter inelastically from D_2 at $E_{coll} = 25$ kcal mol^{-1}. 53

4.8. Representative time-of-flight distributions of reactively scattered OD following reaction of $O(^3P)$ with D_2 at $E_{coll} = 25$ kcal mol^{-1}. 55

4.9. Laboratory angular distribution of the OD product from the reaction of $O(^3P)$ with D_2 at $E_{coll} = 25$ kcal mol^{-1}. 55

4.10. Center-of-mass translational energy distributions for the $O(^3P) + D_2 \rightarrow$ OD +D reaction at $E_{coll} = 25$ kcal mol^{-1}. 56

4.11. Center-of-mass angular distributions for the $O(^3P) + D_2 \rightarrow$ OD +D reaction at $E_{coll} = 25$ kcal mol^{-1}. 56

4.12. Center-of-mass velocity-flux map superimposed on a Newton diagram for the OD product from the reaction of $O(^3P) + D_2 \rightarrow$ OD + D at $E_{coll} = 25$ kcal mol^{-1}. 58

4.13. Center-of-mass velocity-flux map superimposed on a Newton diagram for the OD product from the reaction of $O(^3P) + D_2 \rightarrow$ OD + D at $E_{coll} = 25$ kcal mol^{-1}. 59

4.14. Center-of-mass velocity-flux map superimposed on a Newton diagram for the OD product from the reaction of $O(^3P) + D_2 \rightarrow$ OD + D at $E_{coll} = 25$ kcal mol^{-1}. 60

LIST OF FIGURES - CONTINUED

Figure Page

5.1. Energy diagram for the possible reaction channels in the reaction of $O(^3P)$ with CH_4. 67

5.2. A Newton diagram for the OCH_3 + H channel of the $O(^3P)$ + CH_4 reaction at E_{coll} = 62 kcal mol^{-1}. 69

5.3. Time-of-flight distributions collected at five different mass-to-charge ratios that indicate the formation of oxygen-containing products from the reaction of $O(^3P)$ with CH_4. 73

5.4. Time-of-flight (TOF) distributions of inelastically scattered O (top) and reactively scattered OCH_3 (bottom; detected at m/z=29), collected with the detector angle adjusted to coincide with the direction of the center-of-mass velocity vector, which ranged from 4 to 7° with respect to the oxygen-atom beam direction. 76

5.5. Experimental and calculated excitation functions (cross section vs. collision energy) for the $O(^3P) + CH_4 \rightarrow OCH_3 + H$ reaction. 77

5.6. Saddle point structures associated with the $O(^3P) + CH_4 \rightarrow OCH_3 + H$ reaction. 79

6.1. A Newton diagram for the for the reaction of $O(^3P)$ with CD_4 at E_{coll} = 78 kcal mol^{-1}. 87

6.2. A Newton diagram showing the OH + CH_3 and H + OCH_3 channels of the $O(^3P)$ + CH_4 reacton at E_{coll} = 67 kcal mol^{-1}. 88

6.3. Representative time-of-flight distributions of reactively scattered OH following reaction of $O(^3P)$ with CH_4 at E_{coll} = 67 kcal mol^{-1}. 91

6.4. Laboratory angular distribution of the OH product from the reaction of $O(^3P)$ with CH_4. 91

6.5. Center-of-mass translational energy distribution for the $O(^3P) + CH_4 \rightarrow$ OH + CH_3 reaction at E_{coll} = 67 kcal mol^{-1} derived from the TOF and laboratory angular distributions for m/z = 17 (OH^+) through the forward convolution method. 92

LIST OF FIGURES - CONTINUED

Figure Page

6.6. The solid line is the center-of-mass angular distribution of the OH product from the reaction of $O(^3P) + CH_4 \rightarrow OH + CH_3$ reaction at $E_{coll} = 67$ kcal mol^{-1}, derived from the TOF and laboratory angular distributions for $m/z = 17$ (OH^+) through the forward convolution method. 92

6.7. Center-of-mass velocity-flux map, superimposed on a Newton diagram, for the OH product from the reaction, $O(^3P) + CH_4 \rightarrow OH + CH_3$, at $E_{coll} = 67$ kcal mol^{-1}. 94

6.8. Representative time-of-flight distributions of inelastically scattered CD_4 following collisions with $O(^3P)$ at $E_{coll} = 76$ kcal mol^{-1}. 96

6.9. Laboratory angular distribution of CD_4 that scatters inelastically from $O(^3P)$ with $E_{coll} = 76$ kcal mol^{-1}. 96

6.10. Center-of-mass translational energy distribution for the inelastic scattering of CD_4 from $O(^3P)$ at $E_{coll} = 76$ kcal mol^{-1} derived from the TOF and laboratory angular distributions for $m/z = 20$ (CD_4^+) through the forward convolution method. 97

6.11. Center-of-mass angular distribution of CD_4 product from inelastic scattering from $O(^3P)$ at $E_{coll} = 76$ kcal mol^{-1} derived from the TOF and laboratory angular distributions for $m/z = 20$ (CD_4^+) through the forward convolution method. 97

6.12. Center-of-mass velocity-flux map superimposed on a Newton diagram for CD_4 inelastically scattering from $O(^3P)$ at $E_{coll} = 76$ kcal mol^{-1}. 99

6.13. Representative time-of-flight distributions collected at five different mass-to-charge ratios resulting from $O(^3P)$ colliding with CD_4 at $E_{coll} = 73$ kcal mol^{-1} and at $\Theta_{LAB} = 6.5°$. 100

6.14. Time-of-flight distributions of $m/z = 15$ (CH_3^+) collected at $E_{coll} =$ 67 kcal mol^{-1} in the reaction of $O(^3P)$ with CH_4 (above). Time-of-flight distributions of $m/z = 18$ (CD_3^+) collected at $E_{coll} = 76$ kcal mol^{-1} in the reaction of $O(^3P)$ with CD_4 (below). 101

LIST OF FIGURES - CONTINUED

Figure Page

6.15. Newton diagrams for $O(^3P) + CD_4 \rightarrow OCD_3 + D$, showing the OCD_3 Newton circle (blue). If the OCD_3 undergoes secondary dissociation to OCD_2, its scattering will appear as a second Newton circle (red) with its center-of-mass directly on and all around the OCD_3 Newton circle. 103

6.16. Representative time-of-flight distributions of the OCD_3 product from the reaction of $O(^3P) + CD_4 \rightarrow OCD_3 + D$ at $E_{coll} = 76$ kcal mol^{-1}. 105

6.17. Laboratory angular distribution of the OCD_3 product from the reaction of $O(^3P)$ with CD_4 with $E_{coll} = 76$ kcal mol^{-1}. 105

6.18. The solid line represents the center-of-mass translational energy distribution for the $O(^3P) + CD_4 \rightarrow D + CD_3O$ reaction at $E_{coll} = 78$ kcal mol^{-1}, obtained from the TOF and laboratory angular distributions for $m/z = 30$ (CDO^+) through the forward convolution method. 106

6.19. Center-of-mass angular distribution of the CD_3O product from the reaction of $O(^3P) + CD_4 \rightarrow D + CD_3O$ reaction at $E_{coll} = 78$ kcal mol^{-1}, obtained from the TOF and laboratory angular distributions for $m/z = 30$ (CDO^+) through the forward convolution method. 106

6.20. A Newton diagram for $O(^3P) + CD_4 \rightarrow OCD_3 + D$, showing the OCD_3 Newton circle (blue). If the OCD_3 undergoes secondary dissociation to OCD_2, its scattering will appear as a set of secondary Newton circles (red) with their center-of-masses directly on and all around the OCD_3 Newton circle. 116

ABSTRACT

Hyperthermal reactions of $O(^3P)$ occur at the surfaces and in the exhaust gases of spacecraft that travel through the residual atmosphere of the Earth at high altitudes (200-600 km). These reactions may degrade materials through oxidation and erosion, or they may yield internally excited reaction products which emit radiation and contribute to the "signature" of a rocket plume. Crossed-beams experiments were used to study model reactions of $O(^3P)$ with H_2, D_2, CH_4, and CD_4 at center-of-mass collision energies in the range 8 - 75 kcal mol^{-1}. Interpretation of the experimental results has been strengthened by theoretical calculations carried out by collaborators. A study of the OH scattered flux as a function of collision energy has led to the determination of an experimental excitation function in the threshold region for the $O(^3P) + H_2 \rightarrow OH + H$ reaction. The experimental excitation function clearly matched the theoretical prediction, which confirmed that the laser-detonation source produces $O(^3P)$ atoms. The excitation function for the $O(^3P) + H_2$ reaction and the dynamics of the $O(^3P) + D_2$ reaction, observed experimentally for the first time, demonstrate that these reactions proceed mainly on triplet potential energy surfaces, with little or no intersystem crossing. Experiments on the reactions of $O(^3P)$ with methane have revealed a previously unobserved reaction pathway, which involves H-atom elimination: $O(^3P) + CH_4 \rightarrow OCH_3 + H$. The excitation function for this reaction has been measured, and the reaction barrier has been determined to be ~46 kcal mol^{-1}. In addition, the expected H-atom abstraction reaction, $O(^3P) + CH_4 \rightarrow CH_3 + OH$, has been observed, and the dynamics have been investigated. Theoretical calculations identify a triplet-singlet curve crossing below the triplet barrier for the H-atom elimination reaction, but the observed dynamics indicate reaction exclusively on the two lowest-lying triplet surfaces. While it remains to be seen whether intersystem crossing will affect the outcome of other reactions involving hyperthermal atomic oxygen, unknown reactions which have high barriers are likely to be common in extreme environments such as low-Earth orbit, where spacecraft surfaces and exhaust gases suffer high-energy collisions with ambient atomic oxygen.

INTRODUCTION

Spacecraft in the Low-Earth Orbital Environment

The low-Earth orbital environment, having an altitude range of 200 to 600 km, is host to many short-term and long-term spacecraft, including the International Space Station (350-460 km), space shuttle (~300 km), a large number of private and government satellites, such as communications satellites, and missiles. During their time in low-Earth orbit (LEO) these spacecraft are surrounded by a strongly oxidizing residual atmosphere predominantly composed of atomic oxygen.[1] At typical space shuttle altitudes, the oxygen atom number density is on the order of 10^9 cm^{-3}.[1-3] Most of the oxygen atoms are in the ground, or $O(^3P)$, electronic state, while only 0.001 percent is estimated to be in the first excited state, $O(^1D)$.[2] In addition to the presence of neutral oxygen atoms, there are other neutral species, such as N_2, He, and O_2, with number densities at least ten times lower than the oxygen atoms, and there is also a small ionic component to the LEO atmosphere, of which the most abundant ion, O^+, is 10^4 times less dense than oxygen atoms.[2,4,5]

As spacecraft move in their orbits at relative velocities of about ~7.4 km s^{-1} (accounting for co-rotation of the orbit), they collide with the residual atmosphere.[6,7] At orbital altitudes of ~300-400 km, collisions between the spacecraft surfaces and ambient oxygen atoms have a mean collision energy around 108 kcal mol^{-1}. The roughly 1000 K kinetic temperature[1] of the atmosphere gives an energy spread (full width at half maximum) of ~48 kcal mol^{-1} to the collisions.[7] The collision energy of oxygen atoms striking exhaust plume species released from the spacecraft is not as well defined, as it is heavily dependent on the relative velocity between the two collision partners. The high-energy collisions between oxygen atoms and spacecraft surfaces lead to erosion and oxidation of surface materials, in particular polymers,

compromising the integrity of external surfaces,[8,9] while collisions between spacecraft exhaust species and oxygen atoms result in chemiluminescent products,[10] which have important implications in spacecraft tracking and surveillance, such as identification of the country of origin of a spacecraft or missile. Understanding the chemistry occurring during these high energy, or hyperthermal, collisions of oxygen atoms with spacecraft surfaces and with exhaust plume species is only beginning to be uncovered.

Polymer Erosion in LEO

Energetic collisions of oxygen atoms with spacecraft surfaces are considered to be one of the most important hazards to spacecraft in LEO, because such collisions can lead to eventual failure of exposed materials.[8,9] The detrimental effects of atomic oxygen in LEO were first recognized after post-flight analyses of polymer surfaces that were exposed during the earliest space shuttle flights.[11,12] The polymers showed a loss of surface gloss and concomitant weight loss. Concern over the degradation of materials by atomic oxygen sparked a huge effort, involving space- and ground-based studies, that has been aimed at the identification, understanding, and mitigation of problems caused by atomic oxygen in LEO.[13]

Despite such efforts, uncovering the details of the chemistry behind the oxygen atom erosion of polymers has been a formidable task. Progress towards understanding this chemistry has largely been accomplished, to varying degrees of success, by measuring mass loss during exposure of various polymers to oxygen atoms[14] and studying the chemical structure of the surface before, during, and after exposure.[15] While these approaches provide information about the net result of the complex reactions that are occurring at a polymer surface during exposure to atomic oxygen and allow inferences to be made about the chemical and physical interactions at the surface, they are an insensitive probe of the individual reaction and interaction mechanisms that combine to produce the net result. Experiments can be designed, however,

to study the individual steps of the overall erosion process, from initial interactions of oxygen atoms with a surface (initiation), to oxidation of carbon and scission of the hydrocarbon bond (propagation), and ultimate removal of volatile carbon-containing species (material loss).

Chemiluminescence From O-Atom Reactions with Rocket Plumes

Orbiting spacecraft in and missiles traveling through LEO exhaust plumes of combustion products and unburned fuel when using thrusters to adjust their position in orbit or to maintain their velocity. Other gaseous species, mostly H_2O, may be released from outgassing of materials in the space vacuum. Species within the exhaust plumes, which include fully and partially combusted fuel (including hydrocarbon fuel, in particular CH_4)[10], oxidizer, and possibly other chemical "countermeasures", interact with the ambient oxygen atoms at high center-of-mass (c.m.) collision energies forming internally excited products that produce radiative emissions around the space vehicle. Although some collisions have sufficient energy to form electronically excited products that can emit visible or ultraviolet radiation, it is more common for products to be formed with vibrational and rotational excitation, thus leading to emission of infrared radiation.[10] Both inelastic scattering, $O + X \rightarrow O + X^*$, and reactive scattering, $O + XY \rightarrow OX^* + Y^{**}$, can lead to infrared emissions.[10,16,17] Some efforts have been made to study these interactions in space by optical measurements of rocket firings or fuel dumps, but the experiments are costly and the spectra are extremely complicated by the complex environment.[10,18] More controlled studies can be made in the laboratory wherein identification of the chemical components released by a spacecraft from the spectral signatures can be accomplished by studying the products formed in the collisions and energy partitioning (i.e. electronic, translational, etc.) following the collisions. This information can then be used by theoreticians and modelers to calculate the expected emission spectra. Once the emission

spectra are known, the type of fuel used to propel the spacecraft or the gasses released around the vehicle can be determined. The ability to analyze and identify species in spectral signatures of spacecraft and missile plumes is considered to be a vital component of a modern missile defense.

From LEO to the Laboratory: Simulating Oxygen Atom Reactions Occurring in LEO

Recreating oxygen-atom reactions occurring in the LEO environment for controlled studies in the laboratory is no trivial task. In order to obtain the collision energy range observed in interactions occurring in LEO, experimentalists have two choices, one of which is accelerating a polymer or intact gaseous molecule, in a controlled fashion, to 7.4 km s^{-1} (16,500 mph), exposing it to a beam of thermal $O(^3P)$, and observing reactions occurring upon collision. The other is creating an oxygen atom beam with a velocity of 7.4 km s^{-1}, directing it to react with a stationary polymer surface or other slow-moving molecular collision partner, and making measurements during the collision. While neither option is simple, it is easier to create a high-velocity beam of atoms than accelerate a polymer or intact molecule to such high velocities. Creating a beam of oxygen atoms is an arduous endeavor because of their very high reactivity. Only a few sources of high-velocity oxygen atoms have been developed over the past 20 years. These include the ion neutralization, laser-sustained discharge, electron stimulated desorption, and laser detonation sources. A review of these and other lower energy oxygen atom sources may be found in Ref. 19. Of the sources mentioned, the laser detonation source has a relatively high flux and is well characterized in terms of beam velocity and by-products, such as light and ions. This source is also one of the only sources to be rigorously characterized in terms of the electronic states of the oxygen atoms in the beam; this work will be discussed in Chapter 3 of this thesis. Details on the operation of the laser detonation source are presented in Chapter 2.

Relevant Oxygen Atom Chemistry

Oxygen Atom Reactions with Hydrogen

While the $O(^3P) + H_2 \rightarrow OH + H$ reaction has only minor relevance to plume chemistry and hydrocarbon erosion in LEO, it is an important reaction for determining the electronic state composition of oxygen atoms produced from the laser detonation source without the use of spectroscopic methods, which are currently unavailable in our laboratory. The knowledge of the electronic state composition of the oxygen atom beam is a cornerstone upon which the understanding of all further reactions discussed in this thesis was built. While details of the beam characterization will be discussed in Chapter 3, a brief background on the $O(^3P)$, $O(^1D) + H_2$ reactions will be provided in this section.

Studies on the $O(^3P) + H_2 \rightarrow OH + H$ reaction span nearly 50 years largely because it is a prototype for hydrogen-atom abstraction reactions and is one of the key reactive steps in hydrogen and hydrocarbon combustion. The OH and H products are "simple" to detect experimentally and the reaction is amenable to thorough theoretical probing, offering a wealth of dynamical information, such as abstraction versus insertion mechanisms and curve crossing effects. Efforts to date have involved many theoretical and experimental approaches,[20-37] however, no experiments have been done that directly probe the reaction dynamics. The reason for this knowledge gap in this simple and prototypical triatomic system is partially due to the high reaction barrier, ~9 kcal mol^{-1}, and the small reduced mass of this system. Since the energy available for reaction is the center-of-mass collision energy, which is given by $E_{coll} = \frac{1}{2}\mu v_{rel}^2$, relative velocities near 8 km s^{-1} are required in order the achieve sufficient collision energy for the reaction to occur with thermal H_2. As discussed in the previous section, creating such an oxygen atom beam is an experimental challenge.

An additional experimental difficulty in studying the $O(^3P) + H_2$ reaction is the possible presence of the first electronic excited state of oxygen $O(^1D)$ in the oxygen atom reactant

beam. In contrast to the $O(^3P)$ reactions, the first electronic excited state of atomic oxygen, $O(^1D)$, which lies 45.4 kcal mol^{-1} higher in energy,[38] reacts readily with H_2 to form OH at very low collision energies, so small amounts of $O(^1D)$ in the oxygen atom beam would overshadow OH products from $O(^3P)$. The $O(^1D)$ reaction is exothermic (~41 kcal mol^{-1}) and barrierless,[39] and therefore the reaction cross sections are much larger than the analogous $O(^3P)$ reaction.[34,40] This stark difference in the reactivity of $O(^3P)$ and $O(^1D)$ is utilized in characterizing the electronic state composition of oxygen atoms produced from the laser detonation source discussed in Chapter 3.

Oxygen Atom Reactions with Alkanes

Much has been learned about $O(^3P)$ reactions with alkanes because of their relevance in combustion and atmospheric chemistry. Dynamical studies of oxygen atom reactions with various alkanes have shown that, at near thermal collision energies, an $O(^3P)$ atom typically reacts by abstracting a hydrogen atom to form an OH radical product, similar to the $O(^3P)$ + H_2 reaction.[41-43] Barriers for this reaction range from 5.0 to 8.1 kcal mol^{-1},[44] depending on the type of hydrogen abstracted (primary, secondary, or tertiary). These barriers are also reduced as the size of the hydrocarbon increases. Lower barriers coupled with larger reduced masses make these experiments more accessible to observe experimentally than the $O(^3P)$ + H_2 reaction. Several studies have been performed examining the kinetics and dynamics of hydrogen atom abstraction from various alkanes by $O(^3P)$, including theoretical calculation and experimental determination of reaction rates and vibrational and rotational distributions of the OH product.[41-47] A review of the hydrogen abstraction reaction by $O(^3P)$ from hydrocarbons was recently published by McKendrick *et al.*[45] All of these studies utilized fairly low collision energies conditions.

While it is well established that OH formation is the major channel in the reaction of alkanes with $O(^3P)$ at low collision energies, products, product energy, and angular distributions for reactions at collision energies representative of spacecraft-environment interactions have yet to be examined. It is easy to envision never before seen reaction channels when an oxygen atom reacts with alkanes at high c.m. collision energy, such as hydrogen atom elimination and possibly carbon-carbon bond breakage (in larger alkanes), if the collision energy is above the barriers for these processes. Prior to the work described in this thesis, only one limited theoretical study had considered the high collision energy regime present in LEO: Massa and coworkers performed *ab initio* calculations on the $O(^3P)$ reaction with ethane to form OCH_3 and CH_3 radicals.[48] They found a transition state structure and an activation barrier to the C-C bond breaking mechanism of about 41 kcal mol^{-1}. This channel was the only one considered in their calculations, although several more pathways are energetically possible.

Initial Reactions of $O(^3P)$ with a Hydrocarbon Surface

While it may seem counter intuitive to study reactions of gas-phase alkanes to elucidate mechanisms occurring on a surface, gas-phase-like processes have been observed in collisions of oxygen atoms with a saturated hydrocarbon surface.[19,49,50] In these experiments, which probe only the initial steps of the erosion process, 115 kcal mol^{-1} oxygen atoms were directed at a liquid hydrocarbon surface.[49,50] Only volatile reaction products could be detected in this experiment, and two products were observed: OH, which is formed via hydrogen atom abstraction by an oxygen atom, reminiscent of the gas-phase $O(^3P)$ + alkane reaction, and H_2O, formed from further reaction of the OH radical with the surface. In the formation of the OH product, the oxygen atom is believed to collide with a surface fragment of finite mass in

a localized interaction, similar to the interaction between an oxygen atom and a gas-phase hydrocarbon species. In fact, the effective mass of the surface fragment with which the oxygen atoms collided was found to be about 44 amu, the same mass as a propane molecule. This gas-phase-like formation of OH was determined to be one of the important first steps in the erosion process.

The observation that gas-phase-like reactions are occurring on surfaces led to using gas-phase hydrocarbons as collision partners for the oxygen atoms in order to study the dynamics, instead of the hydrocarbon surface. Reducing the size of the hydrocarbon reaction partner from a liquid, such as used in the experiment discussed above, squalane ($C_{30}H_{62}$), to a gaseous hydrocarbon, for example propane (C_3H_8), should lead to analogous results for the initial reactive events. However, since the alkanes are already in the gas phase, all reaction products formed, including possible oxygen-containing hydrocarbon species, would be detectable using the methods available and their dynamics could be examined. The smaller alkanes serve as excellent model systems to understand the reactions that can occur at surfaces and in spacecraft plumes. Furthermore, unlike the surfaces, these model systems can be treated in depth with modern theoretical methods. Chapters 5 and 6 in this thesis represent the first exploration into the reaction dynamics of hyperthermal atomic oxygen with saturated hydrocarbons by considering the reaction of $O(^3P)$ with the simplest hydrocarbon, methane.

Experiment-Theory Coupling

In the experiments undertaken, theoretical calculations done exclusively by Prof. George Schatz, Dr. Diego Troya, Dr. Biswajit Maiti, and Ronald Pascual at Northwestern University (NU) were invaluable in interpreting the data obtained. For every experiment, calculations were performed by Schatz at various levels of theory to serve not only as an invaluable aid to experimental data interpretation, but to refine codes developed at NU. The ultimate goal in

both of these efforts is to understand how a hydrocarbon polymer erodes in LEO and be able to model it reliably. None of the theoretical calculations herein are to be interpreted as the work of the author.

References

1. K. S. W. Champion, A. E Cole and A. J. Kantor, "Standard and Reference Atmospheres," *Handbook of Geophysics and the Space Environment*, Ed. A. S. Jursa (United States Air Force, Air Force Geophysics Laboratory, 1985).

2. R. G. Roble, "Energetics of the Mesosphere and Thermosphere," *The Upper Mesosphere and Lower Thermosphere: A Review of Experiment and Theory*, Eds. R. M. Johnson and T. L. Killeen (American Geophysical Union, Washington, D.C., 1995) pp. 1-21.

3. J. T. Visentine, "Environmental Definition of the Earth's Neutral Atmosphere," *NASA/ SDIO Space Environmental Effects on Materials Workshop held in Hampton, VA, 28 June - 1 July 1988*, NASA Conference Publication 3035, Part 1, Eds. L.A. Teichman and B.A. Stein (NASA, Washington, D.C., 1989) pp. 179-195.

4. *Natural Orbital Environmental Guidelines for Use in Aerospace Vehicle Development*, Eds. B. J. Anderson and R. E. Smith, NASA Technical Memorandum 4527 (NASA, Washington, D.C., 1994).

5. D. B. Green, G. E. Caledonia, and T. D. Wilkerson, *J. Spacecraft Rockets* **22**, 321 (1988).

6. E. Murad, *J. Spacecraft Rockets* **33**, 131 (1996).

7. B. A. Banks, K. K. deGroh, S. L. Rutledge and F. J. DeFilippo, *Prediction of In-Space Durability of Protected Polymers Based on Ground Laboratory Thermal Energy Atomic Oxygen*, NASA Technical Memorandum 107209 (NASA, Washington, D.C., 1996).

8. L. K. English, *Mat. Eng.* August, 39 (1987).

9. D. E. Hunton, *Sci. Am.* 261, 92 (1989).

10. F. S. Simmons, *Rocket Exhaust Plume Phenomenology* (American Institute of Aeronautics and Astronautics, Inc., Reston, VA, 2000).

11. L. J. Leger and J. T. Visentine, *J. Spacecraft Rockets* **23**, 505 (1986).

12. L. J. Leger, *Oxygen Atom Reaction with Shuttle Materials at Orbital Altitudes*, NASA Technical Memorandum 58246 (NASA, Houston, TX, 1982).

13. L. E. Murr and W. H. Kinard, *Am. Sci.* **81**, 153 (1993).

14. A. F. Whitaker and B. Z. Jang, *J. Appl. Polymer Sci.* **48**, 1341 (1993).

15. D. E. Brinza, S. Y. Chung, T. K. Minton, and R. H. Liang, *Final Report on the NASA/ JPL Evaluation of Oxygen Interactions with Materials-3 (EOIM-3)*, NASA JPL Publication (NASA, Pasadena, CA, 1994).

16. G. E. Caledonia, "Infrared Radiation Produced in Ambient/Spacecraft-Emitted Gas Interactions Under LEO Condition," in *Proceedings of the 38th AIAA Aerospace Sciences Meeting & Exhibit held in Reno, NV, 10-13 January, 2000*, AIAA-00-0104 (AIAA, Reston, VA, 2000).

17. B. L. Upschulte and G. E. Caledonia, *J. Chem. Phys.* **96**, 2025 (1992).

18. L. S. Berstein, Y-H. Chiu, J. A. Gardner, A. L. Broadfoot, M. I. Lester, M. Tsiouris, R. A. Dressler, and E. Murad, *J. Phys. Chem. A*, 107, 10695 (2003).

19. T. K. Minton and D. J. Garton, "Dynamics of Atomic-Oxygen-Induced Polymer Degradation in Low Earth Orbit," in *Advance Series in Physical Chemistry: Chemical Dynamics in Extreme Environments*, ed. R. Dressler (World Scientific, Singapore, 2000).

20. G. Dixon-Lewis and D. J. Williams, *Comp. Chem. Kinet.* **17**, 1 (1977).

21. N. Cohen and K. R. Westberg, *J. Phys. Chem. Ref. Data* **12**, 531 (1983).

22. N. Presser and R. J. Gordon, *J. Chem. Phys.* **82**, 1291 (1985).

23. S. Javoy, V. Naudet, S. Abid, and C. E. Paillard, *Int. J. Chem. Kinet.* **32**, 686 (2000).

24. G. C. Light, *J. Chem. Phys.* **68**, 2831 (1978).

25. J. Han, X. Chen, and B. R. Weiner, *Chem. Phys. Lett.* **332**, 243 (2000).

26. R. E. Howard, A. D. McLean, and W. A. Lester, *J. Chem. Phys.* **71**, 2412 (1979).

27. S. P. Walch, T. H. Dunning, R. Raffenetti, and F. W. Bobrowitz, *J. Chem. Phys.* **72**, 406 (1980).

28. J. S. Wright, D. J. Donaldson, and R. J. Williams, *J. Chem. Phys.* **81**, 397 (1984).

29. T. H. Dunning, Jr., L. B. Harding, A. F. Wagner, G. C. Schatz, and J. M. Bowman, *Science* **240**, 453 (1988).

30. T. Joseph, D. G. Truhlar, and B. C. Garrett, *J. Chem. Phys.* **88**, 6982 (1988).

31. S. Rogers, D. Wang, A. Kuppermann, and S. P. Walch, *J. Chem. Phys.* **104**, 2308 (2000).

32. B. R. Johnson and N. W. Winter, *J. Chem. Phys.* **66**, 4116 (1977).

33. R. Schinke and W. A. Lester, **70**, 4893 (1979).

34. G. C. Schatz, *J. Chem. Phys.* **83**, 5677 (1985).

35. D. C. Chatfield, R. S. Friedman, G. C. Lynch, D. G. Truhlar, and D. W. Schwenke, *J. Chem. Phys.* **98**, 342 (1993).

36. B. C. Garrett, D. G. Truhlar, and G. C. Schatz, *J. Am. Chem. Soc.* **108**, 2876 (1986).

37. A. F. Wagner and J. M. Bowman, *J. Chem. Phys.* **86**, 1976 (1987).

38. M. W. Chase, Jr., C. A. Davies, J. R. Downey, Jr., D. J. Frurip, R. A. McDonald, and A. N. Syverud, *J. Phys. Chem. Ref. Data* **14** (Suppl. 1), 531 (1639).

39. G. C. Schatz, L. A. Pederson, and P. J. Kuntz, *Faraday Discuss.* **108**, 357 (1997).

40. D. J. Garton, T. K. Minton, B. Maiti, D. Troya, and G. C. Schatz, *J. Chem. Phys.* **118**, 1585 (2003).

41. P. Andresen and A. C. Luntz, *J. Chem. Phys.* **72**, 5842 (1980).

42. N. J. Dutton, I. W. Fletcher, and J. C. Whitehead, *Mol. Phys.* **52**, 475 (1984).

43. G. M. Sweeney, A. Watson, and K. G. McKendrick, *J. Chem. Phys.* **106**, 9172 (1997).

44. J. T. Herron, *J. Phys. Chem. Ref. Data* **17**, 967 (1988).

45. F. Ausfelder and K. G. McKendrick, *Prog. React. Kinet. Mech.* **25**, 299 (2000).

46. M. C. Lin, "Dynamics of Oxygen Atom Reactions," in *Advances in Chemical Physics: Potential Energy Surfaces*, Ed. K. P. Lawley (John Wiley & Sons, Ltd., Chichester, Great Britain, 1980) pp. 113-167.

47. X. Liu and A. G. Suits, "The Dynamics of Hydrogen Atom Abstraction From Polyatomic Molecules," in *New Directions in Reaction Dynamics*, Eds. K. Liu and X. Yang (World Scientific, Singapore) to be published.

48. A. Gindulyte, L. Massa, B. A. Banks, and S. K. Rutledge, *J. Phys. Chem. A* **104**, 9976 (2000).

49. D. J. Garton, T. K. Minton, M. Alagia, N. Balucani, P. Casavecchia, and G. G. Volpi, *Faraday Discuss.* **108**, 387 (1997).

50. J. Zhang, D. J. Garton, and T. K. Minton, *J. Chem. Phys.* **117**, 6239 (2002).

METHODS

Crossed Molecular Beams Experiments

Crossed molecular beams methods provide a means to study fundamental gas-phase reaction dynamics under single-collision conditions. Y. T. Lee was a pioneer of "universal detection" in crossed-beams scattering experiments,[1-3] and he demonstrated the power of the crossed-beams method in elucidating the details of bimolecular collision dynamics. In his approach, two atomic or molecular beams are crossed at 90°, and products that scatter from the intersection region are detected with a mass spectrometer detector. The detector uses electron-impact ionization, which allows detection of a wide variety of products (thus the term "universal detection").

The hyperthermal oxygen atom reaction dynamics described in this thesis utilized a third generation crossed molecular beams apparatus based on the Y. T. Lee design.[1] A schematic diagram of the apparatus is shown in Fig. 2.1. A pulsed beam containing hyperthermal atomic oxygen is crossed at right angles by a pulsed supersonic beam of pure hydrogen or methane. Products that scatter from the intersection region are detected with a mass spectrometer detector (which rotates in the plane defined by the two beams) as a function of scattering angle and arrival time in the detector. Once ionized by the Brink-type electron-impact ionizer,[4] the products are mass selected with a quadrupole mass filter and counted with the use of a Daly-type ion counter.[5] The signal levels are always low enough that the detector is operated in a pulse counting mode, where electrical pulses resulting from individual ions emerge from the Daly ion counter and are accumulated as a function of their arrival time by a multichannel scaler. The ion flight time from the electron-impact ionizer to the Daly ion counter is proportional to the square root of the mass-to-charge ratio of the ion, and the

proportionality constant is determined empirically. Determination of the arrival time of neutral products at the electron-impact ionizer requires subtraction of the ion flight time from the time when ion counts are registered on the multichannel scaler. The number of ions generated in the electron-impact ionizer is dependent on the number density of neutral species present. Therefore, at a particular detector angle and mass-to-charge ratio, the mass spectrometer detector measures number density distributions as a function of arrival time, *N(t)*. These distributions are commonly referred to as time-of-flight (TOF) distributions. Integrated TOF distributions as a function of detector angle are called "laboratory angular distributions" and

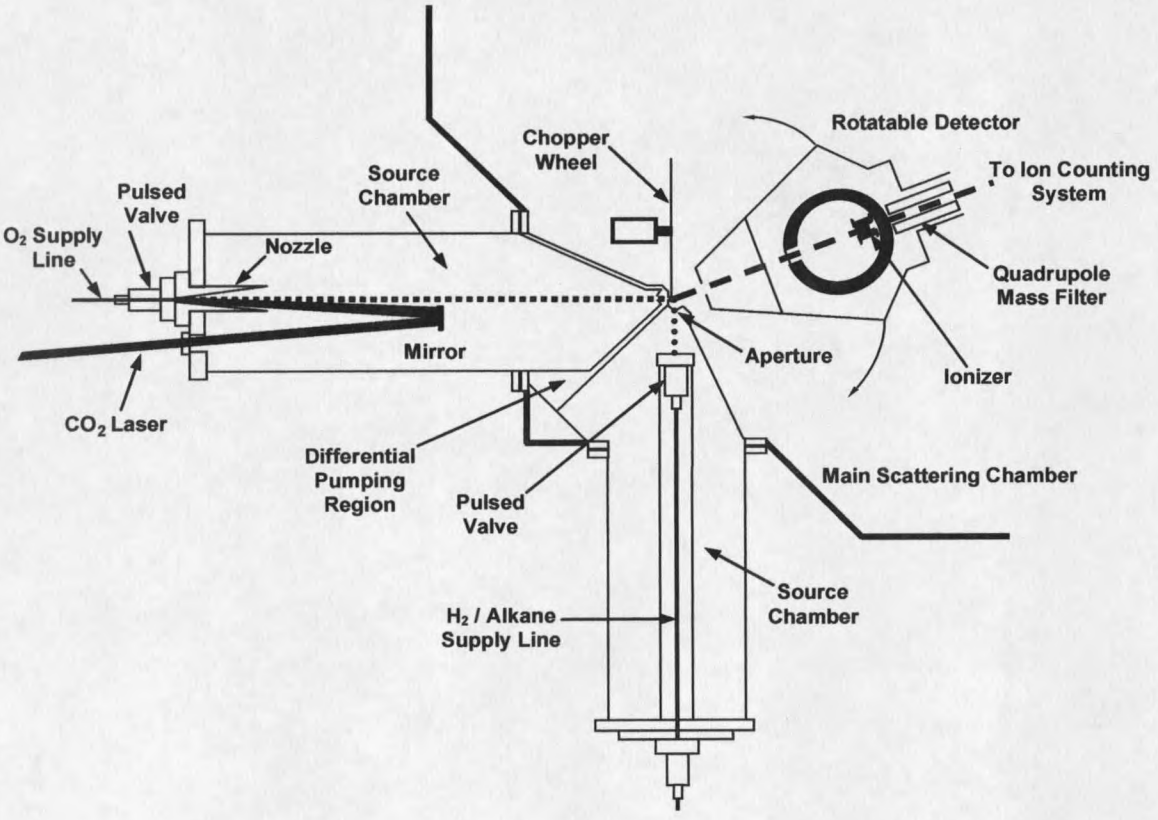

Figure 2.1. Schematic diagram of the crossed molecular beams apparatus at Montana State University. Components of the illustrated apparatus include the laser-detonation hyperthermal beam source, pulsed supersonic H_2/alkane source, differential pumping region, main scattering chamber, and rotatable mass spectrometer detector.

are given the designation $N(\Theta)$, where Θ is the angular direction of the scattered products with respect to the direction of the oxygen-atom beam. (The oxygen-atom beam direction is taken to be a laboratory angle of zero, and the positive angular direction is defined by a rotation from the oxygen-atom beam toward the hydrogen/alkane beam.) The primary data, then, are $N(t)$ and $N(\Theta)$ distributions of mass-selected products. In addition to detecting scattered products, the mass spectrometer detector is used to interrogate the atomic/molecular beams by aligning the detector such that the beam may enter it directly.

Beam Sources

Laser Detonation Source of Hyperthermal Atomic Oxygen

A unique and critical part of the research described herein is the laser detonation source (based on the source invented by Physical Sciences, Incorporated[6,7]), which provides a pulsed beam containing high velocity (6-9 km s^{-1}) oxygen atoms. The key elements of this source are a pulsed piezoelectric molecular beam valve,[8] a gold-plated, water-cooled copper nozzle, and a high energy (~7 J $pulse^{-1}$) CO_2 TEA laser. The pulsed valve introduces a high pressure (250 psig) surge (approximately 100 μs long) of pure O_2 gas into the conical nozzle through a 1 mm diameter × 250 mm long cylindrical channel at the apex of the cone. As the gas begins to expand into the nozzle, the CO_2 laser is fired, and the laser light passes through an antireflection-coated ZnSe window into the source chamber where it is then focused into the nozzle with the use of a bare gold mirror of 1 m radius of curvature. The beam waist of the laser is at the apex of the conical nozzle, but as the beam shape is roughly 4 × 4 mm at the waist, the laser light mainly impinges on the sides of the gold-coated cone and is reflected down into the orifice channel. The concentrated laser pulse initiates a breakdown of the gas and heats the resulting plasma to more than 20,000 K. The high-temperature, high-density

plasma expands rapidly into the 10 cm long, 20° included angle cone following detonation and engulfs the remaining cold gas. The local densities in the nozzle are sufficient to allow for efficient electron-ion recombination, but by the time the majority of the atoms formed in the plasma have cooled enough to recombine, the termolecular collision rate has dropped so low that the atomic species are, in effect, frozen in the emerging beam. Nevertheless, some atoms do recombine before the beam emerges from the nozzle, and the resulting beam thus contains both atomic and molecular oxygen. The ratio of atomic to molecular oxygen is variable depending on various source operating conditions, but the typical atomic fraction is about 70 percent. There is a small ionic component (<<1%), but any residual ions in the experiments described herein were deflected in a magnetic field produced by permanent magnets mounted on the source chamber roughly 50 cm downstream from the nozzle. The laser detonation source is generally operated at a repetition rate of 2 Hz, which is the practical limit allowed by the pumping speed of the source chamber. The pressure in the source chamber rises to ~1 mTorr during the gas pulse.

The hyperthermal beam is first collimated with the use of a 1 cm diameter aperture located 80 cm from the apex of the conical nozzle, and then the beam passes through a region of differential pumping (operating pressure ~10^{-6} Torr) and exits this region through a 3 mm diameter skimmer positioned ~95 cm from the apex of the nozzle. (In one experiment on the $O + D_2$ reaction, a smaller, 1.2 mm diameter, skimmer was used.) The hyperthermal beam reached the interaction region (the center of rotation of the detector) 99 cm from the nozzle apex, where it was only negligibly larger than the diameter of the previous skimmer. The operating pressure in the main scattering chamber was ~2×10^{-7} Torr.

The temporal profile of the atomic oxygen component of the overall hyperthermal beam pulse is seen in Fig. 2.2. The dashed line shows the TOF distribution of atomic oxygen, detected at $m/z = 16$. "Time zero" in this figure is the time at which the CO_2 laser fires, which

is the point in time when the oxygen atoms are created. The ion flight time has been subtracted, so the observed time is the time required for oxygen atoms to travel 132.7 cm from the apex of the nozzle cone to the electron-impact ionizer. As can be seen by the dashed curve in Fig. 2.2, the overall oxygen-atom pulse is very broad. In order to narrow the time (and velocity) width of the oxygen-atom beam pulse, a synchronized chopper wheel is typically used to select only a small portion of the overall beam pulse. This chopper wheel was placed just past the second aperture, in the main scattering chamber. The rotation rate of the chopper wheel was either 270, 300, or 400 Hz for these experiments. Two chopper wheels were used in the experiments, an older chopper wheel with four slots, having a maximum frequency of 270 Hz, and a newer chopper wheel which had three slots, each 1.5 mm wide, currently having a maximum frequency of 400 Hz. Care was taken to fabricate a new chopper wheel that could run stably for an entire day or more, with only a ±200 ns variation in its period. The solid curve in Fig. 2.2 shows the narrowed O-atom beam pulse that was selected with the new synchronized chopper wheel operating at 400 Hz and a final skimmer of 3 mm diameter. Besides defining a narrow oxygen-atom beam pulse, the chopper wheel adds the advantage of blocking all the light from the plasma when the hyperthermal beam was formed.

Supersonic Beam of Hydrogen and Alkanes

A piezoelectric pulsed valve, of the same type as that used for the oxygen-atom source, was used to produce pure beams of molecules (H_2, D_2, CH_4, and CD_4) that served as collision partners for the hyperthermal atomic oxygen. The nozzle orifice diameter was 1 mm, and the pressure behind the orifice was varied from 23 to 80 psig, depending on the gas. Two configurations for the H_2/alkane source were used in the current experiments. In one configuration, a differential pumping region was used between the source chamber and main scattering chamber. In the other configuration, the differential pumping region was removed.

The H_2/alkane beam exited the source chamber (or differential region) through a 1.2 mm diameter skimmer (no differential region) or a 2.5 mm diameter aperture (differential region) located roughly 3 cm from the crossing point of the two beams (interaction region). When the differential region was used, a 5 mm aperture was used between the source and differential chambers, and the distance between this aperture and the second aperture was 2 cm. The distance between the nozzle and first aperture was variable, and for each experiment this distance was set to give optimum scattered signal. Depending on the experiment, various pulse widths were used for the H_2/alkane beam (100 - 650 μs), but in all cases, the duration of the interaction of this beam with the oxygen-atom beam was determined by the temporal width of the oxygen-atom beam, which was less than 15 μs wide (full width at half maximum) at the interaction region. The velocities of the hydrogen and alkane beams were estimated with the use of the formula:[9]

$$\mathbf{v} = \sqrt{\frac{2k_B T}{m}\left(\frac{\gamma}{\gamma - 1}\right)},$$

where $\gamma = C_p/C_v$, T is the nozzle temperature, and m is the mass of the species in the neat beam. The velocity of this beam is probably only accurate to ±10%, but the errors caused by the uncertainty in the H_2/alkane beam velocities are negligible compared to the uncertainties caused by the hyperthermal oxygen-atom beam, which has a nominal velocity that is nearly one order of magnitude larger than and a velocity spread that is almost as large as that of the H_2/alkane beam.

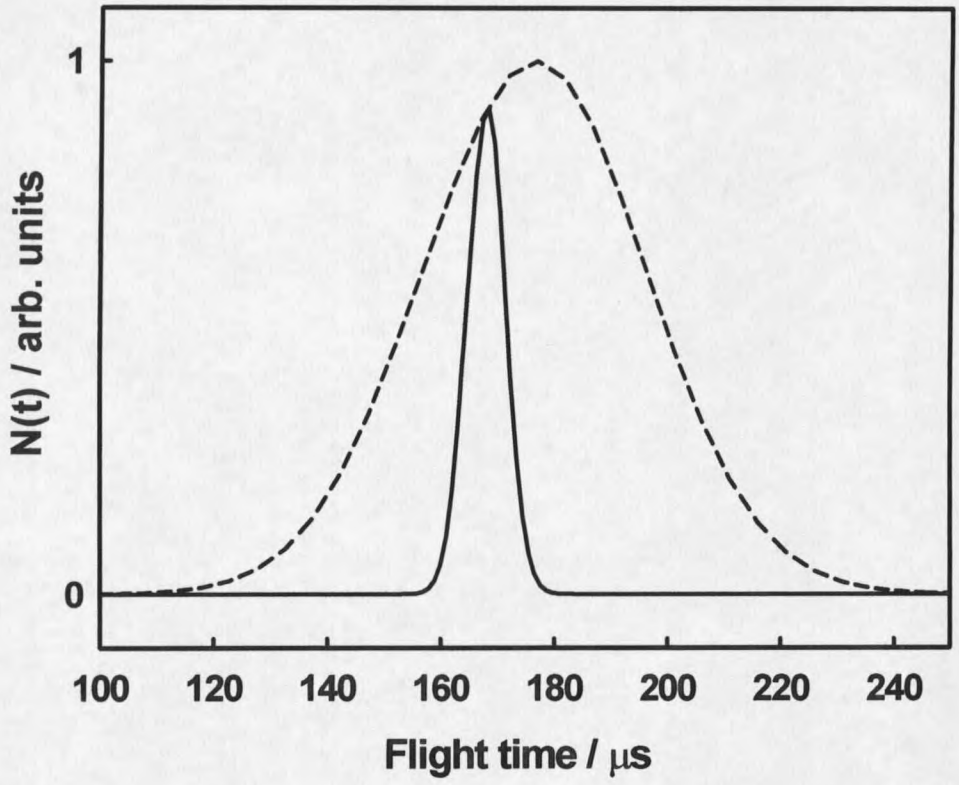

Figure 2.2. Representative oxygen-atom beam time-of-flight distributions. The overall beam distribution (dashed line) was narrowed in all of the experiments with the use of a synchronized chopper wheel. Using a 400 Hz chopper wheel, the beam distribution was narrowed significantly (solid line) and the beam velocity was tunable.

Experiment Timing

Timing is particularly important in pulsed crossed-beams experiments, because the two beam pulses must reach the interaction region at the same time in order for reaction between the two reactant beams to occur. The laser detonation source and associated synchronized chopper wheel impose additional complexity to the timing of the experiments. A timing diagram is shown in Fig. 2.3. The chopper wheel spins at a constant rate and produces a train of pulses as the slots in the chopper wheel pass over an LED/photodiode arrangement. The repetition rate of the experiment is determined by a 2 Hz reference oscillator. The train of

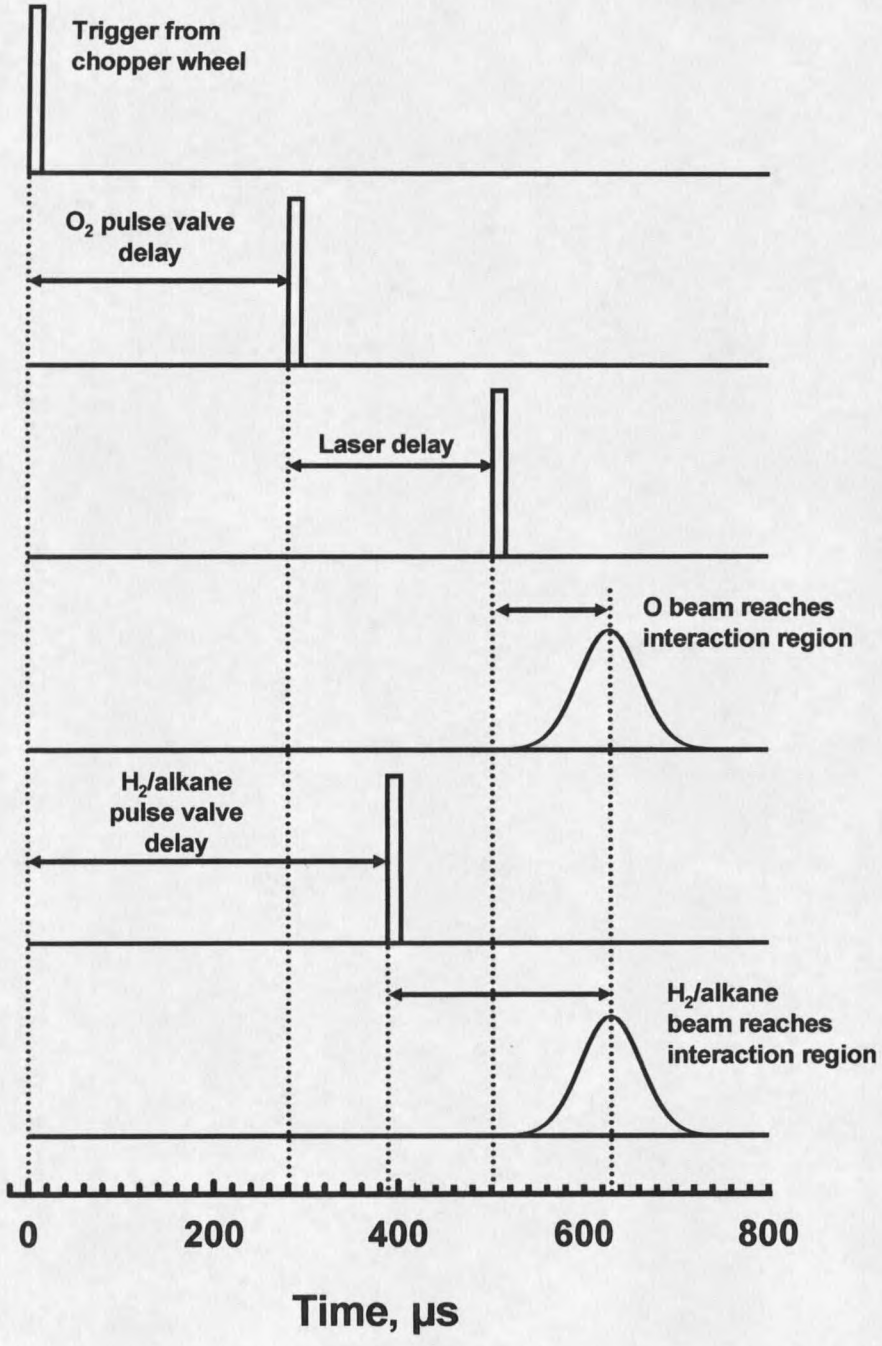

Figure 2.3. Example timing diagram used in the experiments. The timing is set by a chopper wheel placed in front of the oxygen atom beam. All delays are adjusted for each set of experiments.

chopper wheel (photodiode) pulses and the 2 Hz reference pulses are put into a timing circuit that allows the next photodiode pulse following a reference pulse to be output to a digital delay generator. Thus, while the repetition rate is controlled by the 2 Hz reference pulses, the actual experiment timing is controlled by the chopper wheel. The two pulsed valves are triggered at variable, independent delays after the photodiode pulse is received by the delay generator. These delays are labeled in Fig. 2.3 as "O_2 pulsed valve delay" and "H_2/alkane pulsed valve delay." After the O_2 valve is opened, there is a delay of about 200 - 230 μs before the CO_2 laser is fired. The delay generator also controls this "Laser delay." The remaining delays are determined by the flight times of the beam pulses to the interaction region. The laser delay is adjusted to provide the desired nominal oxygen-atom beam velocity. The O_2 pulsed valve delay is adjusted to select the desired portion of the overall oxygen-atom beam pulse with the chopper wheel. And the H_2/alkane pulsed valve delay is adjusted to yield the maximum scattered product signal.

The multichannel scaler is typically triggered by the same pulse that triggers the opening of the O_2 pulsed valve; therefore, measured TOF distributions include the laser delay, the flight time of the oxygen-atom beam pulse to the interaction region, the flight time of neutral products to the electron-impact ionizer, and the ion flight time from the ionizer to the Daly ion counter. The ion flight time is given by $\alpha(m/z)^{1/2}$, where α, which typically has a value of ~2.5, is a parameter that is determined by comparing the raw arrival times of the O and O_2 components of the hyperthermal beam. Because the chopper wheel selects only species in the hyperthermal beam that are traveling at a specific velocity, the difference in raw arrival times of O and O_2 comes from the difference in the ion flight times of O^+ and O_2^+. Thus the ion flight time parameter α is found from the measured difference in the O and O_2 arrival times and the difference in the square roots of the mass-to-charge ratios: $\alpha = \Delta t/\Delta(m/z)^{1/2}$. The flight time of the oxygen-atom pulse from the nozzle cone to the interaction region is

determined by measuring the velocity of the oxygen-atom beam and calculating the time for the beam pulse to travel the known 99 cm distance to the interaction region. The beam velocity is determined by measuring the oxygen-atom flight time – i.e., the time between when the CO_2 laser fires and the time when the beam pulse arrives at the ionizer (132.7 cm away). There is some uncertainty in this measurement, however, because the exact point of origin of the oxygen atoms is not extremely well defined and the pulse width of the laser may be as long as a few microseconds (sharp narrow peak followed by a slow tail). There is thus an estimated uncertainty in the measured flight times of approximately 2 μs. In order to conduct the analysis of the scattered products, their TOF distributions must be corrected such that they reflect the number density distributions of products arriving at the ionizer as a function of flight time from the interaction region. The correction is accomplished by subtracting from the raw TOF distributions: the ion flight time, the oxygen-atom flight time from the nozzle to the interaction region, and the laser delay.

Center-of-Mass to Laboratory Transformation

Both the TOF distributions, $N(t)$, at a fixed angle and the integrated TOF distributions as a function of angle, $N(\Theta)$, contain a wealth of information about the microscopic interactions between the species in the two crossed beams. The measured quantities are number density distributions in the laboratory reference frame, but the relevant microscopic information comes from scattered flux in the center-of-mass (c.m.) reference frame. The two reference frames are different, because the c.m. of the two colliding species is moving in the laboratory frame. The relationship between the c.m. and laboratory velocities can be illustrated with a velocity vector diagram, usually known as a Newton diagram.[9-10] Newton diagrams corresponding to specific reactions studied are presented in the following chapters. While a Newton diagram aids in the determination of c.m. velocities and angles from known laboratory

velocities and angles, it does not provide a means to determine directly c.m translational energy and angular distributions from measured laboratory number density distributions. In fact, because of the complexity of the experiment, including beam velocity distributions, beam angular divergences, ionizer width, and various other apparatus effects, it is extremely difficult (essentially impossible) to deconvolute the measured distributions in order to derive c.m. quantities. Therefore, a "forward convolution" method is typically employed to derive c.m. quantities from the data. The general approach is to start with trial distributions in the c.m. frame and, taking into account apparatus effects, use a Jacobian coordinate transformation to calculate expected laboratory number density distributions and compare these results with the experimental data. In this method, which has been discussed in detail elsewhere,[11-13] the c.m. scattered flux per unit solid angle, $I_{cm}(E_T, \theta)$, is typically assumed to be separable into the product of two functions: a c.m. translational energy distribution, $P(E_T)$, and a c.m. angular distribution, $T(\theta)$, where E_T is the sum of the translational energy of both products which scatter following a collision in the c.m. frame and θ is the angle at which a product scatters in the c.m. frame (with respect to the relative velocity vector of approach of the two collision partners). Trial $P(E_T)$ and $T(\theta)$ distributions are used to calculate TOF distributions with the relationship (derived from a Jacobian transformation),

$$N(t,\Theta) \propto \frac{l^2}{u t^3} I(E_T, \theta) = \frac{l^2}{u t^3} P(E_T) T(\theta),$$

where l is the flight length, u is the product velocity in the c.m. frame, and t is the laboratory flight time. The calculated TOF distributions, which take into account apparatus effects, including the arrival time distribution of the oxygen atoms at the interaction region, are compared with the laboratory TOF and angular distributions, and the input $P(E_T)$ and $T(\theta)$ distributions are iteratively adjusted until optimum fits to all laboratory distributions are obtained. Uncertainties in the derived $P(E_T)$ and $T(\theta)$ distributions are determined by observing

the maximum variation in these distributions that can still produce reasonable calculated fits. In order to allow for easy manipulation of the $P(E_T)$ and $T(\theta)$ distributions, parametrized functions are commonly used. For the current analysis, the $P(E_T)$ distribution was typically based on the versatile RRK form:[12]

$$P(E_T) = (E_T - B)^p (E_{avail} - E_T)^q ,$$

where E_{avail} is the total energy available for translation in the c.m. frame. Thus, E_{avail} is equal to the sum of the c.m. collision energy, E_{coll}, and the reaction energy, ΔE_r. B, p, and q are adjustable parameters that affect the width and the position of the energy maximum in the distribution. An eleven-term Legendre polynomial function, with adjustable weighting of each of the polynomial terms, was used to describe the $T(\theta)$ distribution. The Legendre polynomials can be obtained using Rodrigues' formula:

$$T_k(\theta) = \frac{a_k}{2^k k!} \frac{d^k}{d(\cos(\theta))^k} (\cos^2(\theta) - 1)^k ,$$

where $k = 0, 1, 2,...,10$ (for the 11 total polynomial terms used) and a_k are the coefficients used to adjust the weighting of the terms. By summing over all of the terms, the $T(\theta)$ distribution is obtained.

Once an acceptable fit to the experimental data from the forward convolution simulation is achieved, the $T(\theta)$ and $P(E_T)$ distributions from the forward convolution simulation of the data can be used to create the final outcome of the reactive scattering experiment, the c.m. velocity-flux contour map or differential cross section. This contour map is a plot of the scattered intensity as a function of angle and velocity in the c.m. frame and can be viewed as an image of the reaction.

The computer program used to carry out the center-of-mass to laboratory transformation is the MSU XBEAM Program, Version 2.2, which is derived from the CMLAB program that was originally developed at UC Berkeley in the 1970's and later modified to the GMTHRASH version in the late 1980's and early 1990's. The previous programs were written for crossed beams experiments with continuous beams, so the MSU XBEAM version required significant modification to account for the crossing of pulsed beams,[14] where one of the beams (the oxygen-atom beam) has a distribution of incident times at the interaction region and the atoms arriving at different times have different velocities.

Experimental Resolution

The crossed-beams method used for these experiments is subject to severe limitations in velocity resolution. The product velocity in the laboratory frame is the vectorial sum of the velocity of the center of mass of the two colliding species (in the laboratory frame) and the velocity of the reaction product in the c.m. frame. Because the velocity of the center of mass is high (on the order of 4 km s^{-1}), the product velocities are therefore also high. The product velocities are determined by measuring the product flight time over a 33.7 cm distance. Thus, typical flight times are in the range of 40 - 50 μs. As mentioned previously, there could easily be a 2 μs error in the measurement of the flight time, which would create an error in the laboratory velocity of roughly 400 m s^{-1}, or 5 percent. A compounding source of error is the c.m. velocity, which is only as accurate as the beam velocities. Therefore, the error in the measured laboratory velocities could be as much as 10 percent, which could result in uncertainties in translational energies that are more than 20 percent. Much care must be taken in order to minimize timing errors, because even such a small measurement error of one microsecond can have a large effect on translational energy distributions that are derived from the experiments.

In addition to the uncertainties imparted by the high product velocities, the temporal width of the incident oxygen-atom beam also inhibits velocity resolution and thus the ultimate precision of the derived translational energy distributions. Even with the use of the 400 Hz chopper wheel, the base width of the incident oxygen-atom beam pulse (measured at the detector) was 25 μs, which means that the base width of the product TOF distributions will be at least this much, even if the product translational energy distribution is extremely narrow. The width of the arrival time of the incident beam is accounted for in the analysis, as is the fact that different arrival times correspond to different beam velocities and thus different collision energies. However, when the width of the arrival time distribution accounts for a significant amount of broadening of the product signal, then the energy width of the trial $P(E_T)$ distribution may be varied by many kcal mol^{-1} and have no effect on the calculated TOF distributions. Thus, it becomes difficult to derive a unique $P(E_T)$ distribution. Furthermore, the analysis assumes that over the range of c.m. collision energies resulting from the velocity spread in the oxygen-atom beam, the shape of the $P(E_T)$ distribution of the products will remain constant. This approximation breaks down if the $P(E_T)$ distribution is strongly dependent on collision energy. So, the $P(E_T)$ distribution that is derived represents a sort of average distribution over the range of collision energies in the experiment. In the experiments reported here, it is believed that the width of the arrival time distribution of the incident oxygen-atom beam results in more uncertainty in the derived $P(E_T)$ distributions than does the range of c.m. collision energies.

It is possible to narrow the temporal width of the oxygen-atom beam pulse even further by (1) spinning the chopper wheel faster, (2) reducing the width of the slots in the chopper wheel, or (3) reducing the diameter of the beam as it passes through the chopper wheel. Unfortunately, all of these approaches reduces the beam intensity and thus the signal in the experiment. For the relatively high signal experiment on the reaction of oxygen atoms with

D_2 (see Chapter 4), the diameter of the beam was narrowed in order to improve the time resolution of the experiment. But in all the other experiments reported in this thesis, an improvement in the resolution would have lowered the signals to the point of making the experiments effectively impossible. The choice of chopper slot width and wheel speed was investigated, and it was found more effective to use a wider slot and spin the wheel faster than to use a narrower slot and spin the wheel slower. A possible reason for this observation is that the incident oxygen-atom beam pulse produces a localized pressure increase in the vicinity of a narrow slot, which leads to multiple collisions and a consequent attenuation of the pulse that makes it through the slot. The local pressure does not build up to this extent if the slot width is wider. Another possibility is that scattering from the edges of the slot, again leading to multiple collisions and beam attenuation, is more important for narrower slots than for wider slots. A slot width of 1.5 mm and wheel speed of 400 Hz appeared to be a good compromise, but it was a significant challenge to have a chopper wheel built that could operate very stably in vacuum at this high frequency.

Given the inherent uncertainties associated with the methods employed in the experiments discussed herein, a question arises as to why this method was used instead of another crossed-beams approach, such as velocity map imaging of laser-ionized products.[15-16] Velocity map imaging essentially allows detection of products in the c.m. frame, so the velocity resolution is not so limited by very high laboratory velocities. Moreover, there is the possibility with velocity map imaging to not only identify c.m. angular and translational energy distributions but also internal state distributions of products. The disadvantage of velocity map imaging and other techniques that rely on photon-based detection [single photon ionization, resonance-enhance multiphoton ionization (REMPI), or laser-induced fluorescence (LIF)] is that either the products must be small so the spectroscopy is known (REMPI, LIF) or the light source must be in the vacuum ultraviolet (single-photon ionization). On the other hand, electron-

impact ionization detection is generally applicable to any products that may be formed in a reaction. Ideally, a laboratory for the study of reaction dynamics would have capabilities to conduct both "survey" crossed-beams studies with a rotatable mass spectrometer (or rotatable source and fixed mass spectrometer detector) and velocity map imaging with single-photon ionization for the ultimate in detailed and accurate information. But having both these complementary capabilities would require substantial resources not currently available. And given the fact that the experiments described in this thesis are the first of their kind ever to be performed, it was reasonable to take the approach of universal detection in order to gain the most global knowledge about these heretofore unstudied hyperthermal O-atom reactions.

References

1. Y. T. Lee, J. D. McDonald, P. R. LeBreton, and D. R. Herschbach, *Rev. Sci. Instrum.* **40**, 1402 (1969).

2. Y. T. Lee, J. D. McDonald, P. R. LeBreton, and D. R. Herschbach, *J. Chem. Phys.* **49**, 2247 (1968).

3. Y. T. Lee, J. D. McDonald, P. R. LeBreton, and D. R. Herschbach, *J. Chem. Phys.* **51**, 455 (1969).

4. G. O. Brink, *Rev. Sci. Instrum.* **37**, 857 (1966).

5. N. R. Daly, *Rev. Sci. Instrum.* **31**, 264 (1960).

6. G. E. Caledonia, R. H. Krech, and B. D. Green, *AIAA J.* **25**, 59 (1987).

7. G. E. Caledonia, R. H. Krech, B. D. Green, and A. N. Pirri, *Source of High Flux Energetic Atoms*, Physical Sciences, Inc., US Patent No. 4894511, 1990.

8. D. Proch and T. Trickl, *Rev. Sci. Instrum.* **60**, 713 (1989).

9. J. I. Steinfeld, J. S. Francisco, and W. L. Hase, *Chemical Kinetics and Dynamics, 2nd Ed.* (Prentice Hall, New Jersey, 1999).

10. P. Houston, *Chemical Kinetics and Reaction Dynamics* (McGraw Hill, Boston, 2001).

11. *Atomic and Molecular Beam Methods*, Vol. 1, edited by G. Scoles (Oxford University Press, New York, 1988).

12. R. J. Buss, Ph. D. Thesis, University of California, Berekely (1979).

13. X. Zhao, Ph. D. Thesis, University of California, Berkeley (1988).

14. J. Zhang, Ph. D. Theisis, Montana State University, Bozeman (2001).

15. D. Townsend, M. P. Minitti, and A. G. Suits, *Rev. Sci. Instrum.* **74**, 2530 (2003).

16. X. Liu, R. L. Gross, G. E. Hall, J. T. Muckerman, and A. G. Suits, *J. Chem. Phys.* **117**, 7947 (2002).

EXCITATION FUNCTION FOR THE $O(^3P) + H_2 \rightarrow OH + H$ REACTION: CHARACTERIZATION OF THE OXYGEN ATOM ELECTRONIC STATE IN THE HYPERTHERMAL BEAM

Introduction

The reaction, $O(^3P) + H_2 \rightarrow OH + H$, is of fundamental significance in chemistry, as it is the simplest reaction involving oxygen atoms, one of the key reactions in the combustion of hydrogen and hydrocarbons, and a prototype for hydrogen-atom abstraction reactions. While the reaction has been the subject of numerous investigations beginning in the 1960's, including experimental kinetics studies of rate constants and isotope effects,[1-5] state resolved reaction rates,[6-7] theoretical studies of potential energy surfaces,[8-13] classical trajectory,[14-17] quantum dynamics,[18-23] and transition state theory calculations,[24-27] it has never been studied by molecular beams methods. The reason for this is the high barrier to reaction, 9 kcal mol^{-1}, and small reduced mass, requiring high beam velocities in order to reach sufficient center-of-mass (c.m.) collision energy for the reaction to occur. Additionally, this reaction has very unfavorable kinematics for studying the dynamics experimentally. Figure 3.1 shows a Newton diagram for the reaction, $O(^3P) + H_2 \rightarrow OH + H$, in which the oxygen atom beam velocity is 7900 m s^{-1} and the H_2 beam velocity is 2500 m s^{-1} (representative laboratory conditions). The OH Newton circle is very small and covers a less than 10° range of laboratory angles. Taking into account that the detector viewing angle is ~2°, it is very difficult to obtain angular dependencies of the scattered OH product. Additionally, the small size of the Newton circle inhibits resolution of the forward and backward components of the scattered OH product.

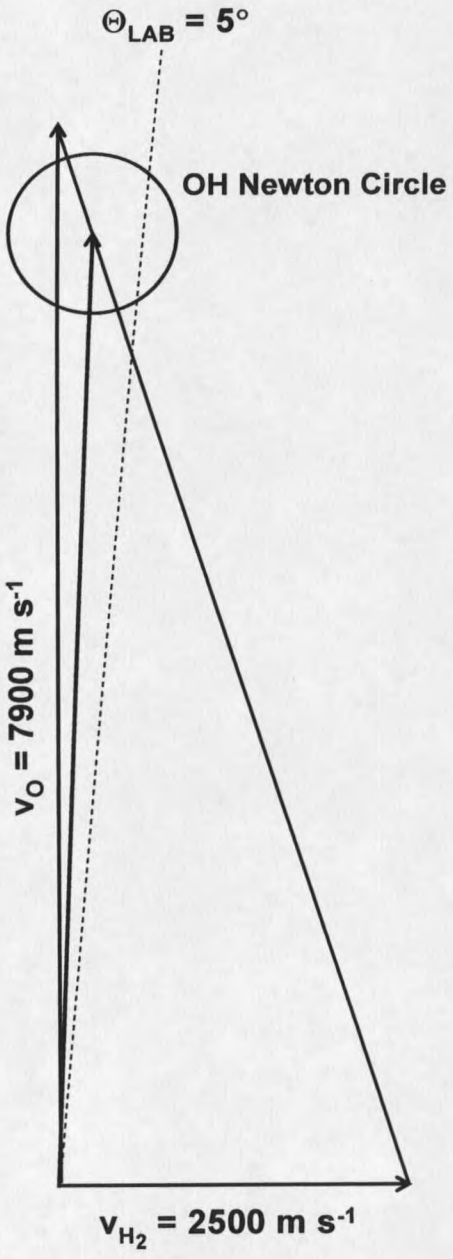

Figure 3.1. Newton diagram for the OH + H channel of the O(^3P) + H_2 reaction at E_{coll} = 15 kcal mol^{-1}. The circle represents the maximum recoil velocity of the OH product given the energy available for reaction, which is the collision energy minus the endoergicity of the reaction.

Despite these unfavorable conditions for obtaining detailed dynamical information, the $O(^3P) + H_2$ reaction is ideal for obtaining a relative excitation function, proportional to reaction cross section as a function of collision energy. The small Newton circle becomes an asset when the primary experimental goal is an excitation function, because the OH flux is scattered over a small region so the detected flux at a fixed detector angle will be representative of the overall reactive product flux.

Although measuring the $O(^3P) + H_2$ excitation function seems experimentally plausible, any $O(^1D)$ in the oxygen-atom beam produced by the laser detonation source would significantly interfere. Since the cross section for the $O(^1D)$ reaction with H_2 is much higher than the $O(^3P)$ reaction in the region of the $O(^3P)$ reaction threshold,[20] OH formed from $O(^1D)$ in the beam would overshadow any OH formed from $O(^3P)$. It is therefore valuable to compare the experimental excitation function with the excitation function predicted by theoretical calculations on the $O(^3P) + H_2$ and $O(^1D) + H_2$ reactions. Very accurate potential energy surfaces (PESs) exist for these reactions, and dynamics calculations involving these PESs, such as excitation function calculations, should be very accurate representations of what will be seen experimentally. We can therefore investigate the possible role that $O(^1D)$ would play in measurements if it were present in an oxygen atom beam by comparing the measured excitation function for $O + H_2$ with calculated cross sections that are based on accurate PESs for both the $O(^3P)$ and $O(^1D)$ reactions with H_2.

Experimental Details

The experiment was performed with the use of the crossed molecular beams apparatus described in Chapter 2. A pulsed beam of hyperthermal oxygen atoms produced in the laser detonation source was crossed by a pulsed supersonic beam of neat H_2 having a nominal velocity of 2.5 km s^{-1}. The hyperthermal oxygen-atom beam pulse was narrowed with the

use of the older, four-slot synchronized velocity selector wheel rotating at 270 Hz. The synchronization between the chopper wheel and the overall beam pulse was varied in order to produce oxygen-atom beams with nominal velocities from 5920 to 10100 m s^{-1}, with velocity widths (FWHM) of 660 to 1800 m s^{-1}. Velocity distributions of the eight different chopped oxygen-atom beams used are shown in Fig. 3.2. The hyperthermal beam nominally consisted of about 70 percent oxygen atoms and 30 percent oxygen molecules, but the relative amounts of O and O_2 varied with the beam velocities; lower velocity beams contained larger fractions of O_2. TOF distributions of products scattered from the crossing region of the two beams were collected at a fixed detector angle of 5° with respect to the oxygen-atom beam, as shown in Fig. 3.1.

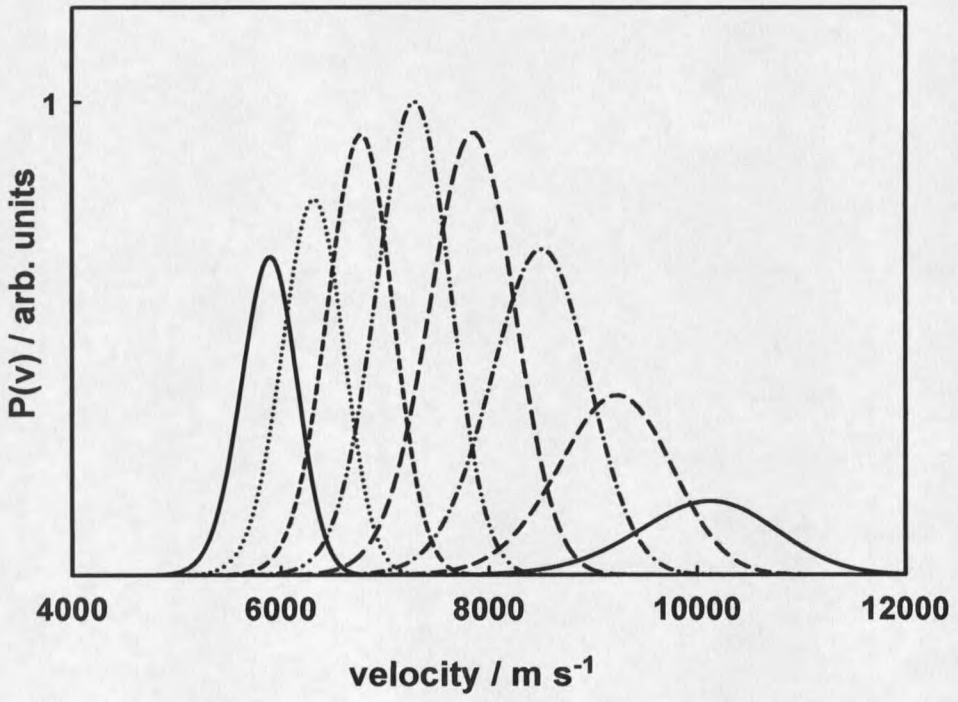

Figure 3.2. Oxygen-atom beam velocity distributions created from chopping the overall beam pulse with a velocity selector wheel rotating at 270 Hz. The synchronization between the chopper wheel and pulsed valve is varied to obtain distributions with different peak velocities.

Results and Analysis

Only inelastically scattered O and reactively scattered OH were detected. Figure 3.3 shows TOF distributions for both O and OH corresponding to eight different nominal center-of-mass (c.m.) collision energies, ranging from 8.8 to 23 kcal mol^{-1}. The signal intensities of the scattered products varied with c.m. collision energy primarily in proportion to the corresponding oxygen atom flux in the hyperthermal beam. In order to obtain the dependence of the scattered OH flux on collision energy, the integrated OH flux at a particular collision energy was divided by the integrated oxygen atom flux at that collision energy. The scattered flux, $I(t)$, is determined from the relationship, $I(t) \propto N(t)/t$, where $N(t)$ is the measured (relative) number density, and t is the flight time from the crossing region of the two beams to the ionizer of the mass spectrometer detector. The integrated flux is thus $\Sigma N(t)/t$. Because the c.m. velocities of scattered O and OH are small compared to the oxygen atom beam velocity, a large fraction of the scattered flux is detected at a single detector angle. Thus, the scattered OH flux as a function of c.m. collision energy should mirror the excitation function for the $O + H_2 \rightarrow OH + H$ reaction. The relative OH flux as a function of collision energy is shown as circles in Fig. 3.4. Within experimental error, the OH flux is zero for a c.m. collision energy of 8.8 kcal mol^{-1}, and the flux rises dramatically as the c.m. collision energy increases to 23 kcal mol^{-1}.

Discussion

Reactive scattering calculations were carried out by Schatz, *et al.* for the same reaction using the $^3A''$ and $^3A'$ analytical potential energy surfaces developed by Rogers *et al.*[13] Dynamics calculations were performed using quasiclassical trajectory (QCT) calculations as well as more accurate time dependent quantum mechanical (TDQM) wave packet methods.[28]

All calculations were done assuming no coupling between the two triplet surfaces, no coupling to any singlet states, and neglecting the 2 ^{3}A″ surface, which would only produce excited products. In order the understand and estimate the role of O(^1D) in the experiment, QCT calculations were performed on the 1 ^{1}A′ and 1 ^{1}A″ analytical potential energy surfaces developed by Dobbyn and Knowles.[29]

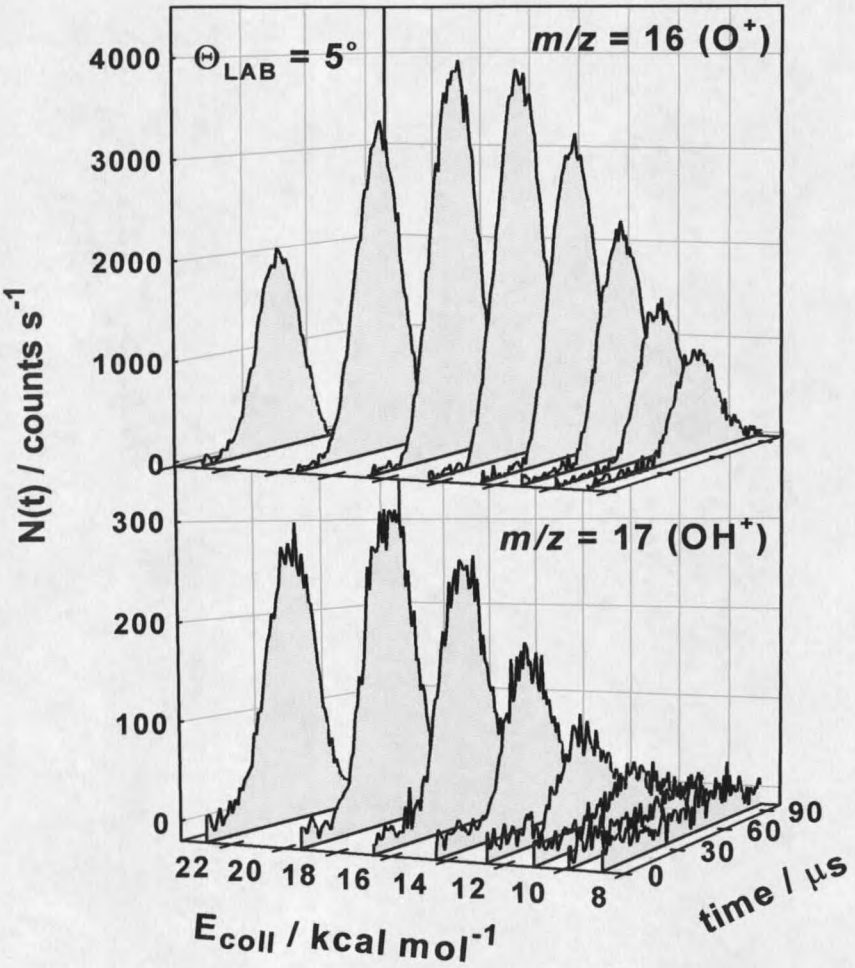

Figure 3.3. Time-of-flight (TOF) distributions of inelastically scattered O (top) and reactively scattered OH (bottom), collected with a detector angle of 5° with respect to the oxygen-atom beam. Eight TOF distributions were collected for both products, corresponding to eight different center-of-mass collision energies, E_{coll}. Time zero in these distributions corresponds to the nominal time at which the oxygen-atom beam pulse intersected the H_2 beam pulse.

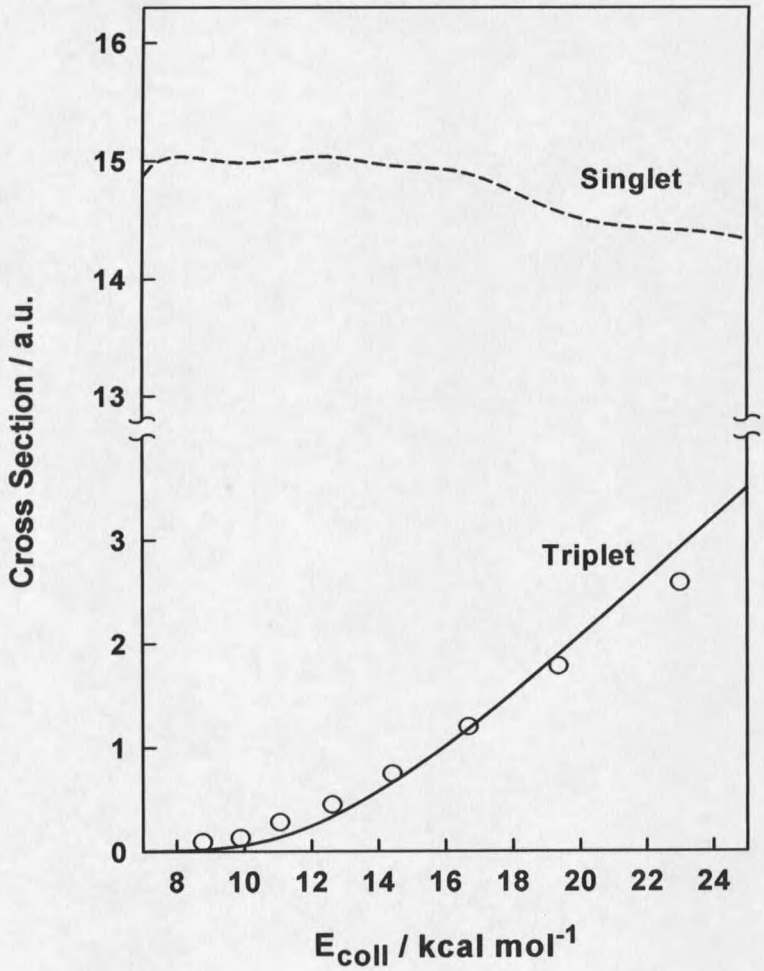

Figure 3.4. Predicted excitation curves (lines) for the $O + H_2$ reaction on singlet and triplet surfaces and experimental data points (circles) for the relative flux of scattered OH product. The predicted curves were determined by averaging the excitation functions shown in Fig. 3.5 [tiplet = ($^3A''$, TDQM + $^3A'$, TDQM)/3; singlet = ($^1A''$, QCT + $^1A'$, QCT)/5] and then convoluting the resulting triplet and singlet curves with the experimental center-of-mass collision energy distributions. Experimental error bars, estimated from the statistical counting errors, are comparable to the size of the circles used to represent the data points.

Figure 3.5 shows the excitation function calculated from the TDQM and QCT methods for both the singlet and triplet surfaces. These results show the threshold near 9 kcal mol^{-1} in the TDQM results for the triplet reaction, which is in stark contrast to the nearly flat singlet cross section (on average) over the same energy range. The QCT results are in good agreement

with the TDQM results for energies more than 2 kcal mol^{-1} above threshold, however close to threshold the TDQM calculations show evidence of tunneling. Results for the two triplet surfaces, which have the same barrier height, are very similar, but, the $^3A''$ surface has somewhat higher reactivity.

The predicted excitation curves for the two reactions, $O(^3P) + H_2$ and $O(^1D) + H_2$, determined by averaging the excitation functions shown in Fig. 3.5 according to the appropriate statistical weight [triplet = ($^3A''$, TDQM + $^3A'$, TDQM)/3; singlet = $^1A''$, QCT + $^1A'$, QCT)/ 5] and then convolving the resulting triplet and singlet curves with the experimental c.m. collision energy distribution, are shown in Fig, 3.4. The experimental OH fluxes, which represent a relative excitation function, have a striking similarity in their dependence on c.m. collision energy to that of the predicted excitation function for the $O(^3P) + H_2$ reaction. Furthermore, the experimental OH flux is zero (within experimental error) at the lowest collision energy of 8.8 kcal mol^{-1}, which is also consistent with reaction on a triplet surface. Given the nearly identical shapes of the experimental excitation function for the $O(^3P) + H_2$ reaction and the fact that the OH flux drops to zero below the predicted threshold for this reaction, we conclude that the dominant reactive species in the hyperthermal beam is $O(^3P)$. The predicted cross sections for the singlet and triplet surfaces and the uncertainty in our data allow us to estimate an upper limit of 1.0 percent for the fraction of $O(^1D)$ in the beam; however, this fraction might in fact be much lower.

Close inspection of the data suggests that the rise in experimental scattered OH flux with collision energy is slightly slower than the predicted rise. This difference is the expected result of the fixed detector angle of 5°. As the collision energy increases, the relative velocity of the O and H_2 increases, and the OH products scatter at higher velocities in the c.m. frame. Therefore, the fraction of products that can be detected at a given lab angle decreases slightly with increasing collision energy, which will tend to reduce effective detection sensitivity as

the collision energy increases. In addition, the fixed detector angle will lead to a slight detection bias toward more sideways c.m. angles as the collision energy increases. The OH product is predicted to be backward scattered (with respect to the c.m. direction of the incident oxygen atoms);[30] thus, a systematic sampling of ever more sideways c.m. angles, as the collision energy is increased, will slightly reduce the rise in measured OH flux from that which would be observed if the detected range of c.m. angles had remained constant. These two systematic errors have only a minor effect on the comparison with the predicted excitation function and no effect on the conclusion that we have observed unequivocal evidence of the $O(^3P) + H_2$ reaction.

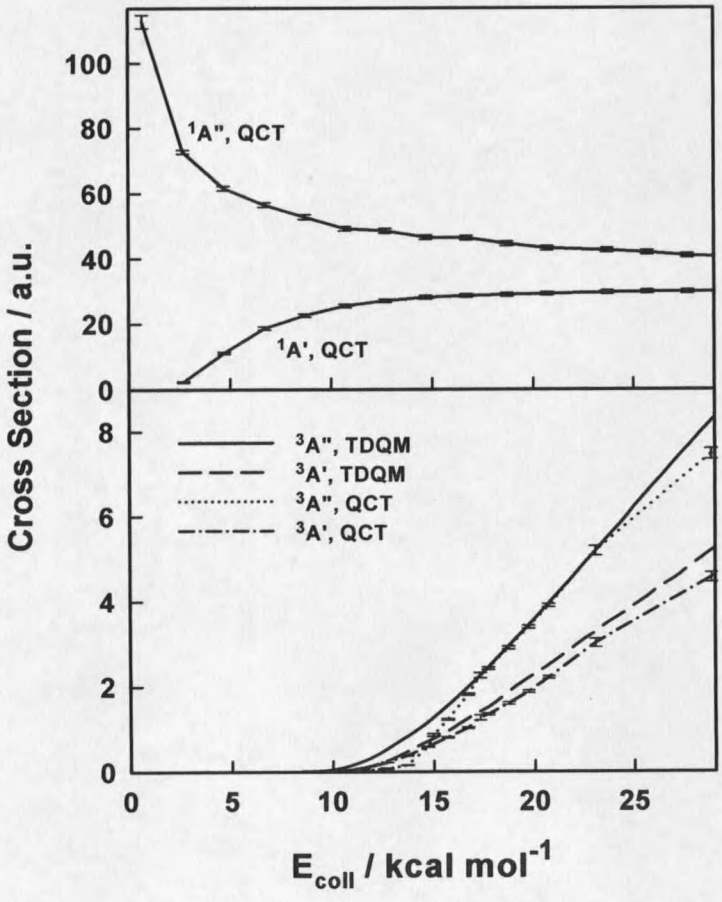

Figure 3.5. Calculated excitation functions from Schatz *et al.* for the $O(^3P) + H_2 \rightarrow OH + H$ reaction. (Top) QCT excitation functions for $O(^1D) + H_2 \rightarrow OH + H$. (Bottom) TDQM and QCT excitation functions for $O(^3P) + H_2 \rightarrow OH + H$.

Conclusion

The excitation function for the reaction, $O(^3P) + H_2 \rightarrow OH + H$, has been investigated with crossed molecular beams methods and has been compared to theoretical excitation functions obtained with accurate quantum wave packet calculations. The close match between experimental and predicted excitation functions leads to the conclusion that the detected OH signal is the result of $O(^3P)$ reacting with H_2. Further quasiclassical trajectory (QCT) calculations yield the excitation function for the reaction, $O(^1D) + H_2 \rightarrow OH + H$, and allow an upper limit of 1.0 percent to be placed on the fraction of O atoms in the beam that are in the excited $O(^1D)$ state. This result suggests that the laser detonation source, which has been used exclusively in this thesis and is often used for simulation of space environmental effects, may be used to create an environment in which the effect of hyperthermal oxygen atoms reflects interactions involving ground-state $O(^3P)$.

References

1. G. Dixon-Lewis and D. J. Williams, *Comp. Chem. Kinet.* **17**, 1 (1977).
2. N. Cohen and K. R. Westberg, *J. Phys. Chem. Ref. Data* **12**, 531 (1983).
3. N. Presser and R. J. Gordon, *J. Chem. Phys.* **82**, 1291 (1985).
4. H.-X. Yang, K. S. Shin, and W. Gardiner, *Chem. Phys. Lett.* **207**, 69 (1993).
5. S. Javoy, V. Naudet, S. Abid, and C. E. Paillard, *Int. J. Chem. Kinet.* **32**, 686 (2000).
6. G. C. Light, *J. Chem. Phys.* **68**, 2831 (1978).
7. J. Han, X. Chen, and B. R. Weiner, *Chem. Phys. Lett.* **332**, 243 (2000).
8. R. E. Howard, A. D. McLean and W. A. Lester, *J. Chem. Phys.* **71**, 2412 (1979).
9. S. P. Walch, T. H. Dunning, R. Raffenetti, and F. W. Bobrowicz, *J. Chem. Phys.* **72**, 406 (1980).
10. J. S. Wright, D. J. Donaldson, and R. J. Williams, *J. Chem. Phys.* **81**, 397 (1984).
11. T. H. Dunning, Jr., L. B. Harding, A. F. Wagner, G. C. Schatz, and J. M. Bowman, *Science* **240**, 453 (1988).
12. T. Joseph, D. G. Truhlar and B. C. Garrett, *J. Chem. Phys.* **88**, 6982 (1988).
13. Rogers, D. Wang, A. Kuppermann, and S. P. Walch, *J. Phys. Chem. A* **104**, 2308 (2000).
14. B. R. Johnson and N. W. Winter, *J. Chem. Phys.* **66**, 4116 (1977).
15. R. Schinke and W. A. Lester, *J. Chem. Phys.* **70**, 4893 (1979).
16. Z. B. Alfassi, and M. Baer, *Chem. Phys.* **63**, 275 (1981).
17. M. Braunstein, S. Adler-Golden, B. Maiti, and G. C. Schatz, *J. Chem. Phys.* **120**, 4316 (2004).
18. D. C. Clary and J. N. L. Connor, *Mol. Phys.* **41**, 689 (1980).

19. J. M. Bowman, and K. T. Lee, in *Potential Energy Surfaces and Dynamics Calculations*; ed. D. G. Truhlar (Plenum, New York, 1981) p. 359

20. G. C. Schatz, *J. Chem. Phys.* **83**, 5677 (1985).

21. K. Haug, D. W. Schwenke, D. G. Truhlar, Y. C. Zhang, J. Z. H. Zhang, and D. J. Kouri, J. *Chem. Phys.* **87**, 1892 (1987).

22. J. M. Bowman, *Chem. Phys. Lett.* **141**, 545 (1987).

23. D. C. Chatfield, R. S. Friedman, G. C. Lynch, D. G. Truhlar, and D. W. Schwenke, *J. Chem. Phys.* **98**, 342 (1993).

24. B. C. Garrett, D. G. Truhlar, R. S. Grev and A. W. Magnuson, *J. Phys. Chem.* **84**, 1730 (1980).

25. B. C. Garrett, and D. G. Truhlar, *Int. J. Quant. Chem.* **29**, 1463 (1986)

26. B. C. Garrett, D. G. Truhlar, and G. C. Schatz, *J. Am. Chem. Soc.* **108**, 2876 (1986).

27. A. F. Wagner and J. M. Bowman, *J. Chem. Phys.* **86**, 1976 (1987).

28. N. Balakrishnan, C. Kalyanaraman, and N. Sathyamurthy, *Phys. Rep.* **280**, 79 (1997); J. Z. H. Zhang, *Theory and Application of Quantum Molecular Dynamics* (World Scientific, Singapore, 1999).

29. A. J. Dobbyn and P. J. Knowles, *Mol. Phys.* **91**, 1107 (1997).

30. R. Schinke and W. A. Lester, Jr., *J. Chem. Phys.* **70**, 4893 (1979).

INELASTIC AND REACTIVE SCATTERING DYNAMICS OF $O(^3P) + D_2$

Introduction

In the previous chapter, the experimental excitation function for the reaction, $O(^3P) + H_2 \rightarrow OH + H$, was measured and compared to very accurate quantum reactive scattering calculations. Two important results emerged from the excitation function study: (1) no intersystem crossing was observed in the reaction of $O(^3P)$ with H_2 at the collision energies under investigation, and (2) less than one percent of the oxygen atoms in the beam produced via laser detonation were in the excited $O(^1D)$ state. The absence of $O(^1D)$ in the beam opened up the possibility of examining the dynamics of many $O(^3P)$ reactions at high relative velocities, with confidence that $O(^1D)$ reactions would not interfere with the experimental results. The first system chosen for study was the $O(^3P) + D_2$ reaction, because it could be modeled very accurately by theoretical methods. In addition, the OD product from this reaction scatters at higher velocities in the c.m. frame than the OH product from the $O(^3P) + H_2$ reaction (for a given relative velocity of the collision); thus the kinematics of the $O(^3P) + D_2$ system are more favorable for investigating the dynamics of the $O(^3P)$ + hydrogen reaction. A Newton diagram showing $O(^3P)$ scattering from D_2 inelastically (O) and reactively (OD) is presented in Fig. 4.1.

Although the dynamics of the $O(^3P) + H_2 \rightarrow OH + H$ reaction have been studied in detail theoretically,[1-13] there are no previous experimental investigations of the dynamics of this reaction. As mentioned before, the primary reason for the paucity of data on the dynamics of this reaction this is the high relative velocity required to overcome the ~9 kcal mol^{-1} barrier. Many experiments and calculations have been done on the $O(^1D) + H_2 \rightarrow OH + H$ reaction, however, which is virtually barrierless.[14-19] These studies have revealed that the OH product

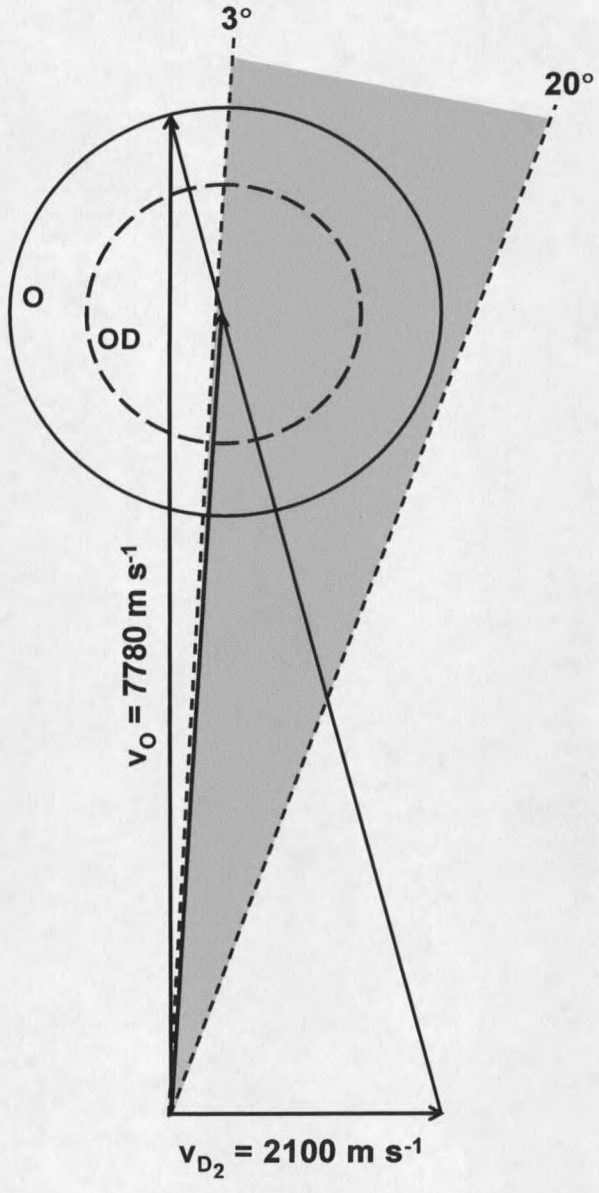

Figure 4.1. A Newton diagram showing inelastically scattered O and reactively scattered OD from hyperthermal collisions of O(^3P) with D_2 at E_{coll} = 25 kcal mol^{-1}. The angular range in gray represents the range of laboratory detection angles used. The circles represent the maximum recoil velocity of the O (solid line) and OD (dashed line) given the energy available for reaction. The available energy for the inelastic scattering is the collision energy, while the available energy for the reaction to form OD is the collision energy minus the endoergicity of the reaction (~2.3 kcal mol^{-1}).

angular distribution is forward-backwards symmetric, with low vibrational and relatively high rotational excitation of the OH product.[17] The reaction occurs mostly on the ground state (^{1}A′) surface. In contrast, recent calculations on the reaction of O(^3P) with $H_2(v)$ have predicted mostly backwards scattering for $v = 0$ and 1, shifting to more forward scattering as the initial vibrational energy of the H_2 increases.[20] This shift in scattering behavior has been attributed to the increasing importance of higher impact parameters as the vibrational quantum number increases.[7] As mentioned in the previous chapter, the two lowest lying surfaces, ^{3}A′ and ^{3}A″, are the only triplet surfaces that lead to formation of ground state OH($^2\Pi$). The third triplet state, 2^3A″, is known to lead only to electronically excited products, which are not energetically accessible in our experiments.

A very important feature of the O + H_2 potential energy surfaces (PESs) is the presence of crossings between the low-spin singlet surface and the high-spin triplet surface. Although the singlet surface starts off much higher in energy (~45 kcal mol^{-1}), it possesses a deep potential well, causing it to cross over to the lower energy triplet surfaces. Hoffmann and Schatz have found that the most important singlet-triplet crossings (for nonlinear O–H–H geometries) involve the two triplet states correlated to the OH($^2\Pi$) product and the lowest O(^1D) + H_2 surface, ^{1}A′.[21] Figure 4.2 shows potential energy curves along the minimum energy path of the reaction for slightly bent O–H–H geometries in both the adiabatic (top) and diabatic (bottom) representations.[22] These curves, which are derived from full dimensional potential energy surfaces and CASSAF spin-orbit couplings, show a singlet-triplet crossing just before the top of the triplet barrier. The small energy gap between the singlet and triplet adiabats indicates weak spin-orbit coupling in the system. It therefore appears that intersystem crossing (ISC) from the triplet to the singlet surfaces is possible, but it has not yet been observed experimentally. There are two experimental studies in which reactions involving O(^3P) led to ISC: (1) Casavecchia *et al.*[23] saw intersystem crossing in the a crossed-beams

reactive scattering study of the O(^3P) with CH_3I reaction and (2) Naaman and coworkers[24,25] observed evidence of ISC in reactions of O(^3P) with hydrocarbon clusters and thin organic films, wherein insertion of the oxygen atom was observed instead of abstraction. While the first example contained a heavy atom which is believed to facilitate ISC,[23] the second example demonstrated the possibility to observe ISC without the presence of heavy atoms.

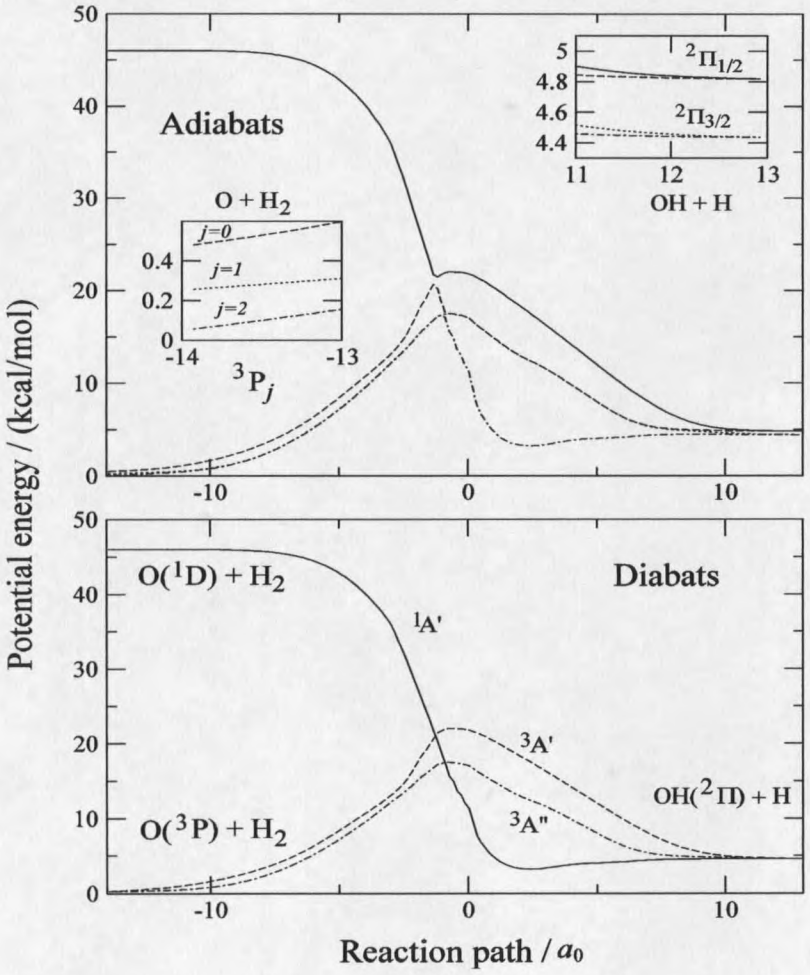

Figure 4.2. Potential energy curves along the minimum energy path for the triplet reaction with H_2 at slightly bent O-H-H geometries (Jacobi angle of 30°). The surfaces ($^1A'$, $^3A'$, and $^3A''$) that correlate to the ground state OH($^2\Pi$) product and that are involved in intersystem crossing are shown. (The collinear geometry has a lower minimum energy path, but no crossings occur.) The top plot shows the adiabatic representation, while the bottom plot shows the diabatic representation. This figure was provided by G. C. Schatz *et al.*

In this chapter, the dynamics of inelastic scattering of $O(^3P)$ from D_2 are explored, as are the dynamics of the only reactive channel, formation of OD. The presence of ISC at these high collision energies is also investigated.

Experimental Details

Experiments were performed on the crossed molecular beam apparatus described in Chapter 2. A pulsed beam of oxygen atoms produced in the laser detonation source and having a nominal velocity of 7780 m s^{-1} was crossed with a pulsed supersonic beam of pure D_2 gas having a nominal velocity of 2100 m s^{-1}. A synchronized 400 Hz chopper wheel was used for velocity selection of the overall oxygen atom beam pulse. Products scattering from the crossing region of the two beams were detected with a rotatable quadrupole mass spectrometer detector.

The oxygen-atom beam exited the source region through a 1 cm diameter skimmer, traveled through a differential pumping region held around 10^{-6} torr, and passed through a second 1.2 mm diameter skimmer before entering the main scattering chamber. The D_2 beam traveled through a 2 mm diameter skimmer into a differential pumping region and then through a 2.5 mm diameter aperture. The main scattering chamber was held at 2×10^{-7} torr throughout the experiment. The oxygen-atom beam produced by the laser detonation source consisted of 63 percent oxygen atoms and 37 percent O_2. As shown in Chapter 3, the oxygen atoms are mostly in the ground, or ^3P, electronic state, with less than one percent (and perhaps no population at all) in the first excited state, ^1D. The oxygen-atom beam distributions were obtained under two detector conditions, both with the D_2 beam off. For one distribution, the detector was placed directly on axis (0°) and for the other the detector was placed at +3° off the oxygen atom beam axis (toward the D_2 beam axis). This served to verify the beam velocity, and also the off-axis beam provided a beam time-of-flight (TOF) distribution under

the same conditions that the scattered products were detected. Products that scattered from the crossing region traveled 33.7 mm to the electron bombardment ionizer in the detector. Ions were selected with a quadrupole mass filter and the resulting ion signals were amplified and counted using a Daly ion counter and multichannel scaler.

Inelastic scattering signals were detected at m/z = 16 (O^+) and 32 (O_2^+). The range of detector angles for which data were collected was based on the Newton diagram shown in Figure 4.1, and varied for detected masses. Signals for m/z = 16 (O^+) were detected at laboratory angles from +3° to +20°. Signals for m/z = 32 (O_2^+), used to corrected the m/z = 16 data for the contribution of cracking of O_2 to O in the ionizer, were detected from +3° to +10° (O_2 did not scatter appreciably to larger angles). Reactive product signals were detected only at m/z = 18 (OD^+) and at laboratory angles of +3° to +12.5°. Counting times varied from 12.5 min for collection of the m/z = 16 and 32 data to 1.4 h for m/z = 18.

Results and Analysis

TOF and laboratory angular distributions were collected for m/z = 16 (O^+), 18 (OD^+), and 32 (O_2^+) at a collision energy, E_{coll}, of 25 kcal mol^{-1}. The Newton diagram in Fig. 4.1 shows the maximum recoil velocity of O and OD given the available energy. For inelastic scattering of oxygen atoms, the available energy is the collision energy (25 kcal mol^{-1}). However, for the reactive scattering to form OD, the maximum energy available for translation is the collision energy minus the endoergicity of the reaction (25 - 2.3 kcal mol^{-1}), or 22.7 kcal mol^{-1}. Scattered O_2 is not included in the Newton diagram since the only purpose for its collection was to correct for its contribution (from dissociative ionization) to the TOF distributions detected at m/z = 16.

Inelastic Scattering

Figure 4.3 shows TOF distributions for $m/z = 16$ collected at six laboratory angles. The TOF distributions at 3° - 10°, where signal was observed for $m/z = 32$, were corrected for the contribution of O_2 cracking to O in the ionizer. This was done by subtracting 11 percent of the signal at $m/z = 32$ (after correction for the ion flight time difference between O and O_2) from the signal at $m/z = 16$. The laboratory angular distribution, or integrated signal as a function of angle, for the oxygen atom inelastic scattering is shown in Fig. 4.4. The solid line in both Figs. 4.3 and 4.4 is the forward convolution simulation to the data based on the c.m. translational energy and angular distributions in Figs. 4.5 and 4.6. These translational energy and angular distributions, which were derived from the experimental TOF and laboratory angular distributions, were very similar to quasiclassical trajectory (QCT) calculation results for $O + D_2 \rightarrow O + D_2$ scattering at $E_{coll} = 25$ kcal mol^{-1} performed by Schatz *et al.* The QCT calculations were run on analytical potential energy surfaces (PES) for the $^3A'$ and $^3A''$ states developed by Rogers *et al.* for reaction of $O(^3P)$ with H_2,[5] and c.m. translational energy and angular distributions were extracted from the trajectory data. Both the $^3A'$ and $^3A''$ surfaces gave nearly identical results for inelastic scattering. The major differences between the c.m. distributions derived from the experimental data and the QCT results for both surfaces were in the widths of the two distributions. The QCT results for the translational energy distribution fell to zero around 22 kcal mol^{-1}, as opposed to ~18 kcal mol^{-1} in the experimentally derived translational energy distribution. The angular distribution also fell more sharply in the QCT. The general results from the QCT calculations and the experimentally derived distributions were the same, showing forward scattering of the oxygen atoms, with very little energy transferred into the D_2 collision partner. The simulation provides reasonably good agreement with the data in Figs. 4.3 and 4.4; however, it must be noted that due to the fairly low resolution of the data, the simulated "fits" are not entirely unique. Small changes in the c.m.

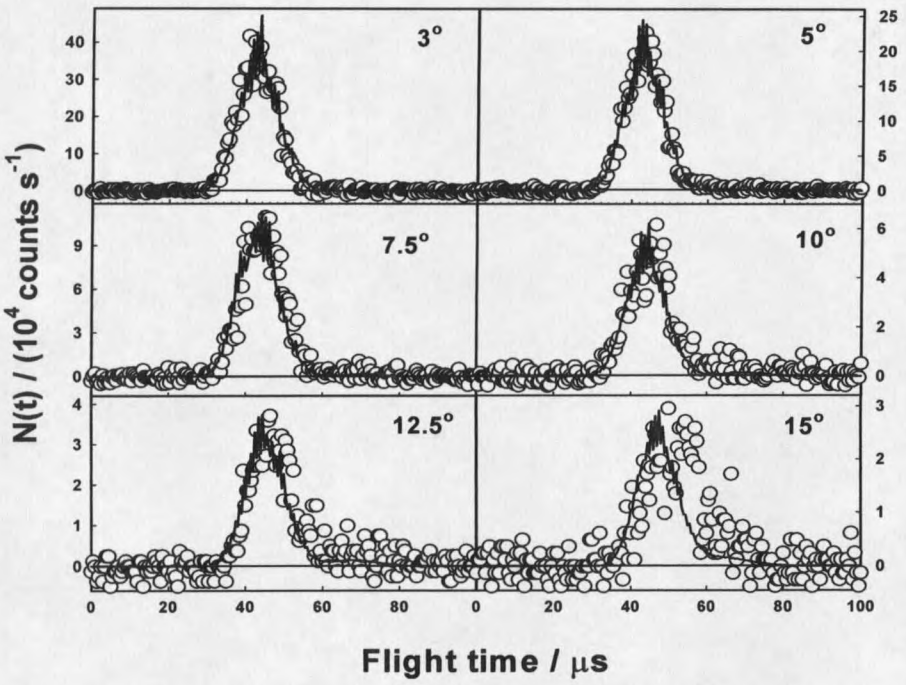

Figure 4.3. Representative time-of-flight distributions of inelastically scattered O following collisions with D_2 at E_{coll} = 25 kcal mol^{-1}. The open circles are the experimental data. The solid line is the forward convolution simulation to the data, derived from the c.m. translational energy and angular distributions in Figs. 4.5 and 4.6.

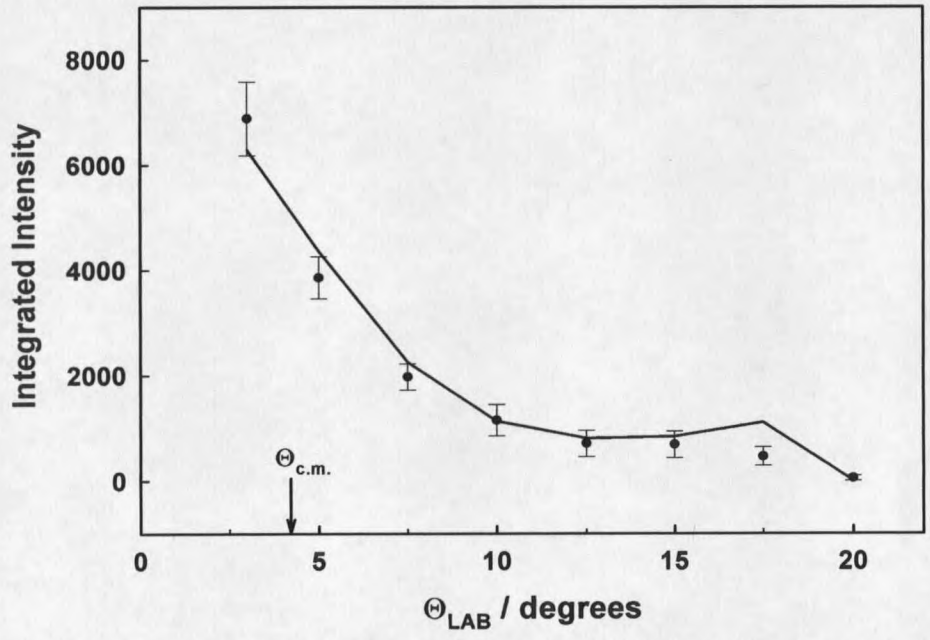

Figure 4.4. Laboratory angular distribution of m/z = 16 (O^+) inelastically scattered from D_2 with E_{coll} = 25 kcal mol^{-1}. The circles are the experimental data, and the solid line is the forward convolution fit to the data.

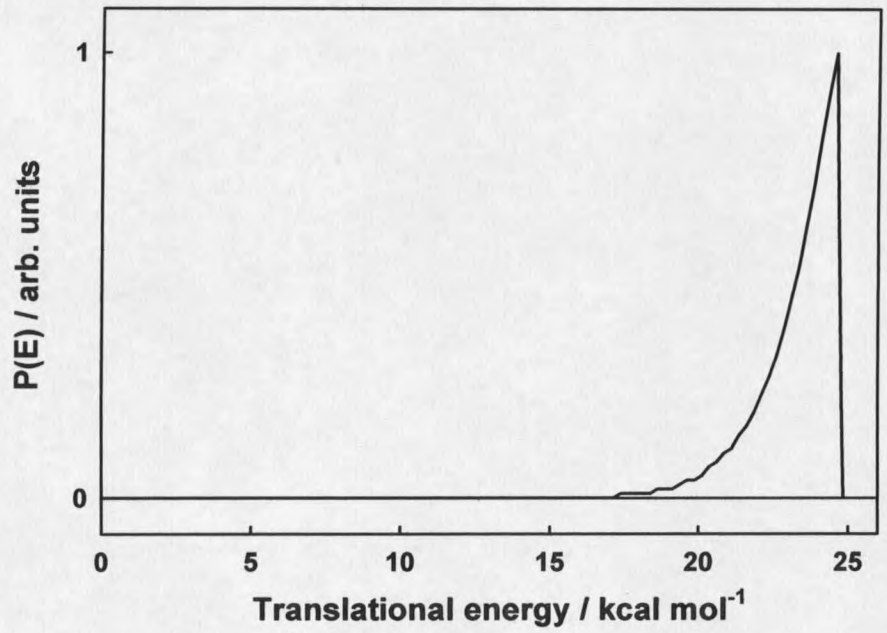

Figure 4.5. Center-of-mass translational energy distribution for the inelastic scattering of O from D_2 at E_{coll} = 25 kcal mol^{-1}, derived from the TOF and laboratory angular distributions for m/z = 16 (O^+) through the forward convolution method.

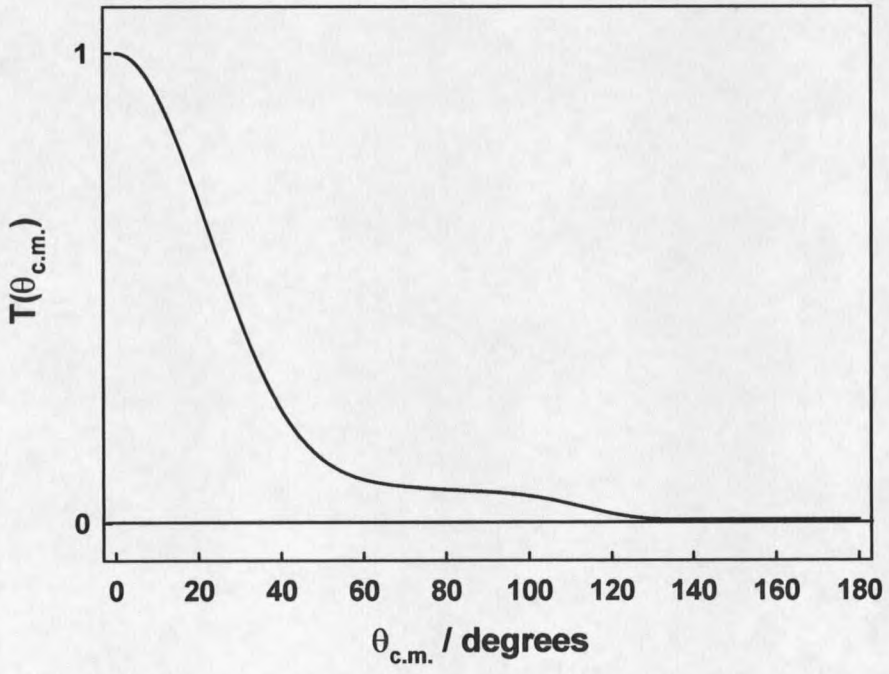

Figure 4.6. Center-of-mass angular distribution for O atoms that scatter inelastically from D_2 at E_{coll} = 25 kcal mol^{-1}, derived from the TOF and laboratory angular distributions for m/z = 16 (O^+) through the forward convolution method.

translational energy and angular distributions will still result in acceptable "fits" to the data. For example, the translational energy distribution for the inelastic scattering of O from D_2 can be broadened slightly, while keeping the peak near 25 kcal mol^{-1}, and the fit to the laboratory TOF and angular distributions is not greatly affected. On the other hand, large changes, altering the character of the generated c.m. distributions, show significant deviations from the simulated results. This insensitivity of the experimental data to small changes in the c.m. distributions is the result of high product velocities and, especially, the temporal width of the incident oxygen-atom beam distribution, which inhibits velocity resolution and thus the accuracy of the derived c.m. distributions. Although the velocity resolution is lower than would be desired, there are limits within which to work. (The error associated with the simulations will be explored in more detail in the following section.) While we cannot achieve perfect "fits" to the data because of limited resolution, we can make general statements about the nature of the scattering in the c.m. frame, such as scattering direction and energy transfer. A c.m. velocity flux map, created from the two experimentally derived c.m. distributions for oxygen atom inelastic scattering, is shown in Fig. 4.7.

Reactive Scattering

Representative TOF distributions of the only reactively scattered product observed, OD, collected at laboratory angles of 3°, 7.5°, 12.5°, and 15° are shown in Fig. 4.8. The distributions at 3°, 5°, and 7.5° had to be corrected for the contribution of ^{18}O that scattered inelastically from D_2. This correction was done by multiplying the scattering signal at $m/z = 16$ (O^+) for each angle by 0.002 (0.2 percent ^{18}O, which was measured by scattering oxygen from helium and looking at the scattered signal at $m/z = 16$ (O^+) and $m/z = 18$ ($^{18}O^+$) in a separate experiment), shifting by the appropriate ion flight time, and subtracting it from the TOF distributions collected at $m/z = 18$. This correction was negligible (less than one count) at

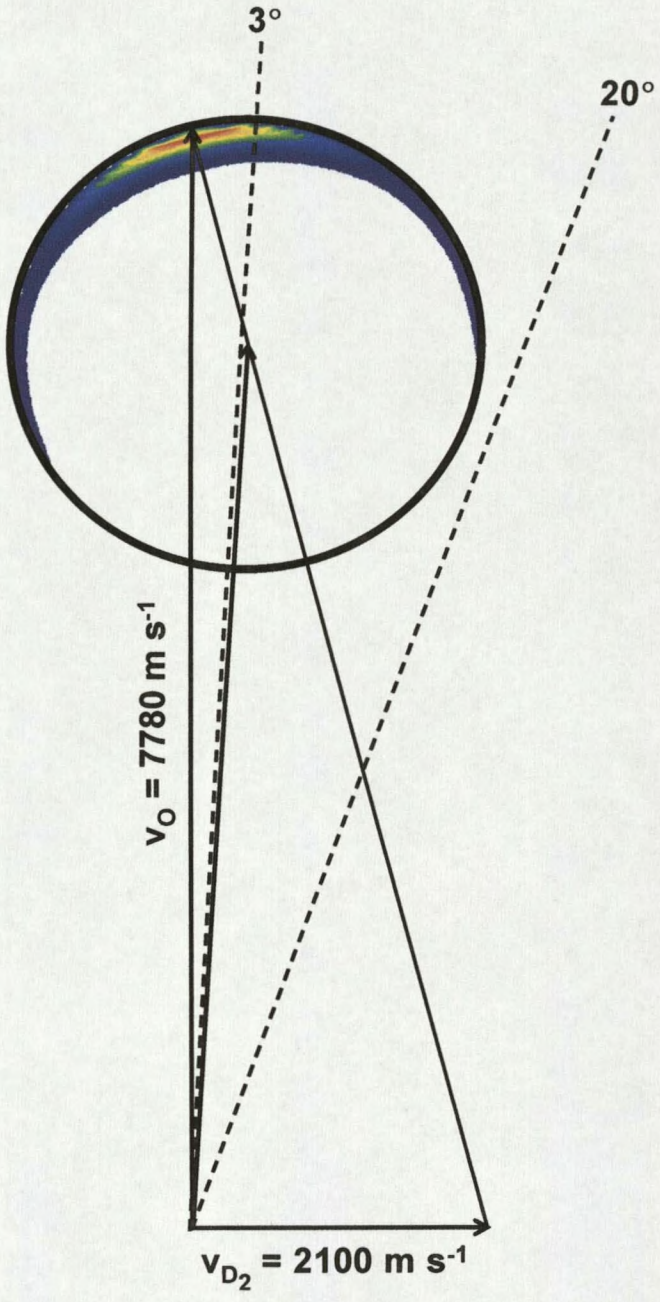

Figure 4.7. Center-of-mass velocity-flux map superimposed on a Newton diagram for O atoms that scatter inelastically from D_2 at E_{coll} = 25 kcal mol^{-1}. The translational energy and angular distributions in Fig. 4.5 and 4.6 were used to create this velocity-flux contour map. Scattered intensity is maximum in the forward direction (indicated by the red color).

angles greater than 7.5°, and so these angles were not corrected for ^{18}O contributions. Laboratory angular distributions are shown in Fig. 4.9. The three curves in each plot represent three different "fits" to the data, one using the results of QCT trajectory calculations and two from c.m. translational energy and angular distributions that gave reasonable fits to all the data. Multiple c.m. distributions were used, in order to investigate carefully the sensitivity of the data to different c.m. functions. The black curves in Figs. 4.8 - 4.11 are the results of high quality single surface QCT calculations performed by Schatz *et al.* on the two triplet surfaces ($^3A'$ and $^3A''$) that correlate to the OD + D products in the ground electronic state. (The third surface is very repulsive and leads to the formation of excited state products that would not be accessible with the collision energies used in the experiment. This surface was therefore not included in the trajectory studies.) Center-of-mass translational energy and angular distributions for the $O(^3P) + D_2 \rightarrow OD + D$ reaction were obtained from the trajectory calculations. Forward convolution of the c.m. distributions obtained from these triplet-only trajectory calculations allowed conversion of the data into the laboratory frame and gave predicted TOF and laboratory angular distribution. These results (black curves) were compared with the experimental data in Fig. 4.8 and 4.9, and seem to provide acceptable fits to the TOF distributions in Fig. 4.8, but they do not show very good agreement with the laboratory angular distribution in Fig. 4.9. The inability of the QCT results to fit the laboratory angular distributions prompted us to try different c.m. translational energy and angular distributions, in order to improve the agreement between the c.m. and laboratory distributions. The red and green curves in Fig. 4.8 - 4.11 are c.m. distributions that provide the superior fits to the data. However, as both curves provide good "fits" to the data, they also show the problem of "uniqueness" in the forward convolution simulation to the data. The red and green curves in Fig. 4.10 have a maximum near the same energy and are quite different in shape, but they are similar in the total energy range they cover. And both of the experimentally derived

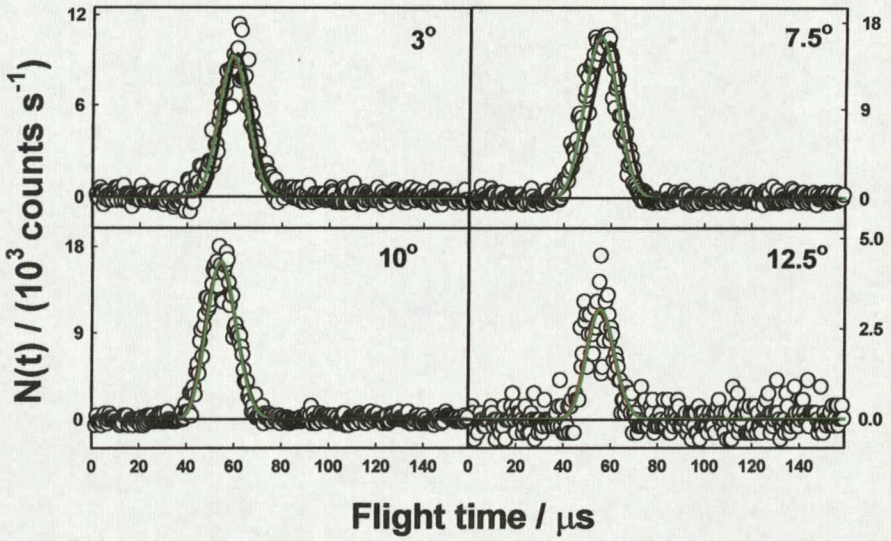

Figure 4.8. Representative time-of-flight distributions of reactively scattered OD following reaction of O(^3P) with D_2 at E_{coll} = 25 kcal mol^{-1}. The open circles are the experimental data. The solid lines show three different results from forward convolution simulation of the data, derived from c.m. distributions shown in Figs. 4.10 and 4.11. The black line shows the results from quasiclassical trajectory calculations (also shown in black in Figs. 4.9, 4.10, and 4.11). The green and red lines show two different results obtained from forward convolution of the corresponding c.m. distributions shown as green and red curves, respectively, in Figs. 4.10 and 4.11. Where red and green lines overlap, a green line is shown.

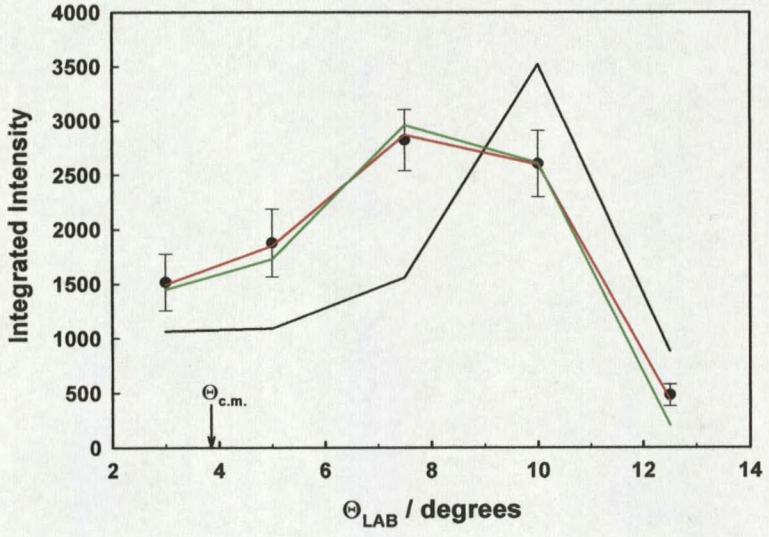

Figure 4.9. Laboratory angular distribution of the OD product from the reaction of O(^3P) with D_2 at E_{coll} = 25 kcal mol^{-1}. The black dots are the experimental data. The error bars are estimated from fitting the TOF distributions with a modified gaussian function and finding maximum and minimum acceptable fits by adjusting the gaussian parameters. The integrated range of these fits are shown as error bars.

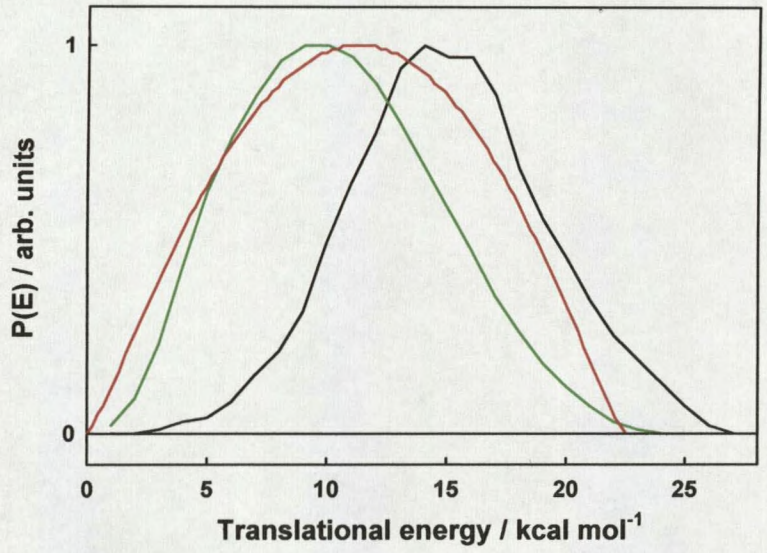

Figure 4.10. Center-of-mass translational energy distributions for the $O(^3P) + D_2 \rightarrow OD + D$ reaction at $E_{coll} = 25$ kcal mol^{-1}. The black curve is the translational energy distribution from quasiclassical trajectory calculations by Schatz *et al.* The green and red curves are two seperate "fits" derived from the TOF and laboratory angular distributions for $m/z = 18$ (OD^+) through the forward convolution method. The green and red curves represent the degree of error in simulating the experimental data.

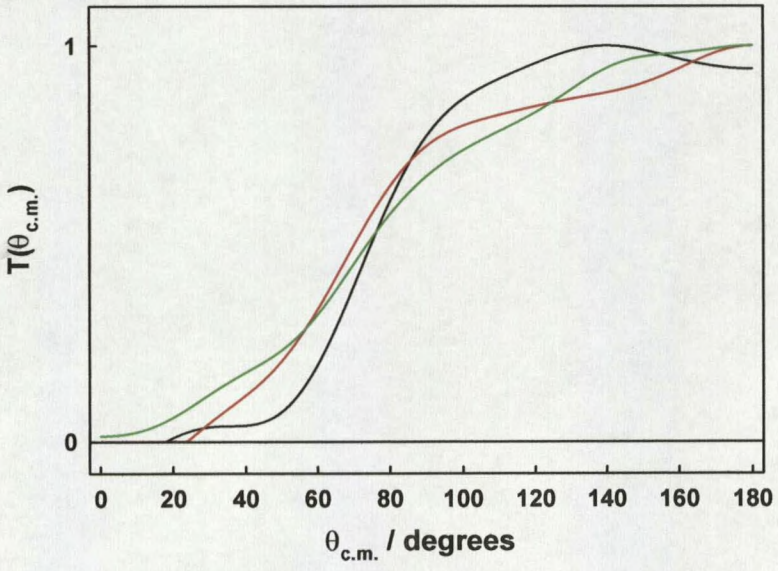

Figure 4.11. Center-of-mass angular distributions for the $O(^3P) + D_2 \rightarrow OD + D$ reaction at $E_{coll} = 25$ kcal mol^{-1}. The black curve is the angular distribution from quasiclassical trajectory calculations by Schatz *et al.* The green and red curves are two seperate "fits" derived from the TOF and laboratory angular distributions for $m/z = 18$ (OD^+) through the forward convolution method. The green and red curves represent the degree of error in simulating the experimental data.

translational energy distributions (red and green curves) have maxima at lower energies than that of the distribution from the QCT calculations. The c.m. angular distributions, shown in Fig. 4.11, corresponding to the red and green translational energy distributions, show similar features, such as a preponderance of backwards scattering and very little forward scattering. Both the experimentally derived c.m. angular distributions are also similar to the distribution obtained from the QCT calculations. The three different c.m. translational energy and angular distributions thus provide an effective error range for the forward convolution simulation procedure. We can draw general conclusions about the scattering based on the three "fits". All three c.m. angular distributions show a large backward scattered peak. The presence of forward scattered OD is difficult to determine with the resolution of the data, but it is possible that there is a small amount of forward scattered OD. We can also determine that there is a broad range of energy transferred into the recoiling OD fragment, and on average ~50 percent of available energy for reaction (E_{coll} - ΔE_r) goes into internal energy of the OD. The inability of the QCT results to predict the laboratory angular distribution suggests that the maximum energy in the translational energy distribution is overestimated. A velocity-flux maps created from the three different sets of translational energy and angular distributions from Figs. 4.10 and 4.11 are shown in Figs. 4.12 - 4.14.

Discussion

The inelastic and reactive scattering events resulting from collisions of $O(^3P)$ with D_2 exhibit significantly different dynamics. For both the inelastic and reactive scattering experiments, results have been compared with high quality triplet-only QCT calculations provided by Schatz *et al.* In the case of inelastic scattering, experimental results showed that oxygen atoms scatter from D_2 with little change in direction and translational energy. The c.m. translational energy distribution for the oxygen atoms has a maximum near the c.m.

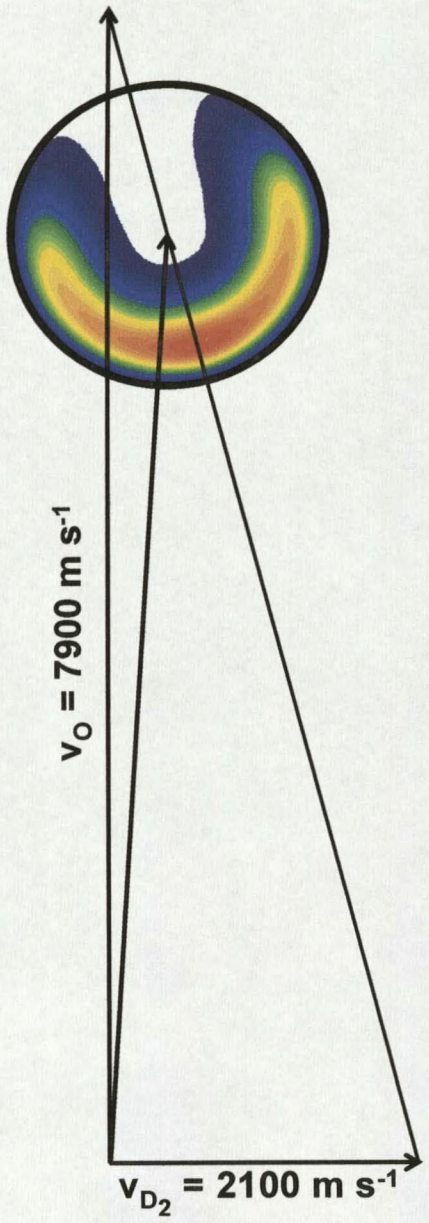

Figure 4.12. Center-of-mass velocity-flux map superimposed on a Newton diagram for the OD product from the reaction of $O(^3P) + D_2 \rightarrow OD + D$ at $E_{coll} = 25$ kcal mol^{-1}. This velocity flux map was created using the red translational energy and angular distributions in Figs. 4.10 and 4.11.